Thick dyke emplacement and internal flow: A structural and magnetic fabric study of the deep-seated dolerite dyke of Foum Zguid (southern Morocco)

Pedro F. Silva, Fernando O. Marques, Bernard Henry, Pedro Madureira, Ann M. Hirt, Eric Font, Nuno Lourenço

Thick dyke emplacement and internal flow: A structural and magnetic fabric study of the deep-seated dolerite dyke of Foum Zguid (southern Morocco)

Pedro F. Silva,[1,2] Fernando O. Marques,[2] Bernard Henry,[3] Pedro Madureira,[4] Ann M. Hirt,[5] Eric Font,[2] and Nuno Lourenço[2,6]

Received 14 April 2010; revised 6 August 2010; accepted 9 September 2010; published 30 December 2010.

[1] Knowledge on forced magma injection and magma flow in dykes is crucial for the understanding of how magmas migrate through the crust to the Earth's surface. Because many questions still persist, we used the long, thick, and deep-seated Foum Zguid dyke (Morocco) to investigate dyke emplacement and internal flow by means of magnetic methods, structural analysis, petrography, and scanning electron microscopy. We also investigated how the host rocks accommodated the intrusion. Regarding internal flow: 1. Important variations of the rock magnetic properties and magnetic fabric occur with distance from dyke wall; 2. anisotropy of anhysteretic remanent magnetization reveals that anisotropy of magnetic susceptibility (AMS) results mainly from the superposition of subfabrics with distinct coercivities and that the imbrication between magnetic foliation and dyke plane is more reliable to deduce flow than the orientation of the AMS maximum principal axis; and 3. a dominant upward flow near the margins can be inferred. The magnetic fabric closest to the dyke wall likely records magma flow best due to fast cooling, whereas in the core the magnetic properties have been affected by high-temperature exsolution and metasomatic effects due to slow cooling. Regarding dyke emplacement, this study shows that the thick forceful intrusion induced deformation by homogeneous flattening and/or folding of the host sedimentary strata. Dewatering related to heat, as recorded by thick quartz veins bordering the dyke in some localities, may have also helped accommodating dyke intrusion. The spatial arrangement of quartz veins and their geometrical relationship with the dyke indicate a preintrusive to synintrusive sinistral component of strike slip.

Citation: Silva, P. F., F. O. Marques, B. Henry, P. Madureira, A. M. Hirt, E. Font, and N. Lourenço (2010), Thick dyke emplacement and internal flow: A structural and magnetic fabric study of the deep-seated dolerite dyke of Foum Zguid (southern Morocco), *J. Geophys. Res.*, *115*, B12108, doi:10.1029/2010JB007638.

1. Introduction

[2] Although there has been extensive work on magma flow and propagation of dykes, most works have been carried out on shallow dykes (mainly in volcanic islands) where a passive infilling of tensile fractures is expected [e.g., *Knight and Walker*, 1988; *Gudmundsson*, 2006; *Hildenbrand et al.*, 2008]. Close to the surface, magma can flow almost freely through open fractures, but deeper in the crust, magma slowly makes its way up through rocks with no open fractures. By studying dykes that cooled at different depth with different thickness, one can investigate how magma flows under different conditions, mostly because viscosity and cooling depend on depth; that is, greater depth correlates with higher temperature and lower viscosity, and thickness, whereby thicker dykes cool more slowly. Some questions still persist on how the magma forces its way up through the crust, how the magma flows within thick intrusions, and how the host rocks accommodate the mechanical, thermal and chemical processes associated with the intrusive process. In order to answer these questions we investigated the thick, deep-seated doleritic Foum Zguid dyke (FZD, southern Morocco) and its host sedimentary rocks. We carried out an extensive collection of oriented paleomagnetic samples along several cross sections perpendicular to the FZD and its host rocks, in a total of seven

[1]Departamento de Engenharia Civil, Instituto Superior de Engenharia de Lisboa, Lisbon, Portugal.
[2]Instituto Dom Luís, Universidade de Lisboa, Lisbon, Portugal.
[3]Paléomagnétisme, Institut de Physique du Globe de Paris, CNRS, Saint-Maur, France.
[4]Departamento de Geociências, Centro de Geofísica de Évora, Universidade Évora, Evora, Portugal.
[5]Laboratory of Natural Magnetism, Institute of Geophysics, ETH Zurich, Zurich, Switzerland.
[6]Estrutura de Missão para a Extensão da Plataforma Continental, Paco de Arcos, Portugal.

0148-0227/10/2010JB007638

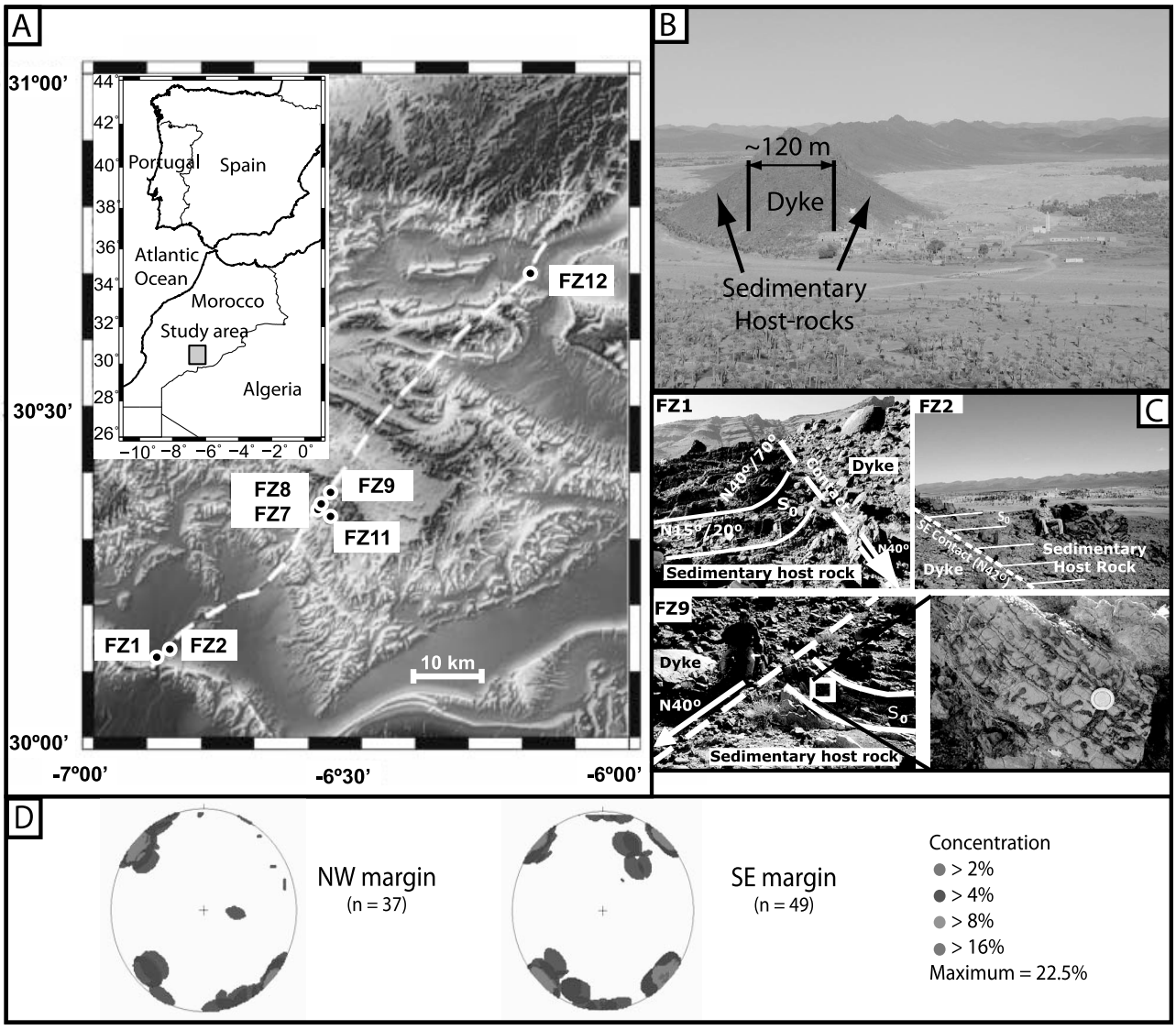

Figure 1. (a) Geographical location of the study area with studied stations. Dashed line represents the main igneous body; (b) photo of the Foum Zguid dyke (topographic high) with indication of its thickness and contacts with sedimentary host rocks; (c) photographs of outcrops. Examples from stations FZ1 and FZ9 illustrate examples of folded bedding close to the contact; FZ2 exemplifies planar bedding orthogonal to the dyke; (d) density diagrams of the poles of the preferential planar discontinuities measured along the dyke margins of the southernmost segment of the dyke between stations FZ1 and FZ9 (stereographic projection in the lower hemisphere).

stations (Figure 1a) and 450 samples. Cross sections cover distances between the first few centimeters to tens of meters from the contacts. The petrofabric of igneous and host sedimentary rocks was evaluated by measurement of anisotropy of magnetic susceptibility (AMS), and its meaning supported by anisotropy of anhysteretic remanent magnetization (AARM) analysis and magnetic zone axis determination. The present study also includes detailed rock magnetic, structural and microscopic, including scanning electron microscopy–energy dispersive spectroscopy (SEM-EDS), analyses.

[3] Following the pioneering works of *Graham* [1954] and *Khan* [1962], AMS has been successfully applied as a tool to assess petrofabric of metamorphic [e.g., *Borradaile and Henry*, 1997; *Hirt* et al., 2000; *Silva et al.*, 2001; *Borradaile and Jackson*, 2004; *Chadima et al.*, 2006; *Almqvist et al.*, 2009], igneous [e.g., *Hrouda et al.*, 1999; *Herrero-Bervera et al.*, 2002; *Henry et al.*, 2009], particularly dykes [*Knight and Walker*, 1988; *Moreira et al.*, 1999; *Callot et al.*, 2001; *Borradaile and Gauthier* 2003; *Krasa and Herrero-Bervera*, 2005; *Aubourg et al.*, 2008], and sedimentary rocks [e.g., *Tarling and Hrouda*, 1993; *Raposo et al.*, 2006; *Cifelli et al.*, 2009].

[4] AMS records the preferred orientation-distribution of all minerals (i.e., diamagnetic, paramagnetic, and ferromagnetic), due to grain shape anisotropy or crystallographic control on magnetic properties. Thus, the orientation of the AMS ellipsoid could represent a potential magma flow

indicator if the rocks have not been later affected by tectonic deformation [*Raposo and Berquó*, 2008]. Otherwise, AARM and partial AARM (pAARM), which are sensitive to the domain state of remanence-bearing minerals, enables the identification of the preferred orientation of subpopulations with distinct size and shape. The comparison between AMS and AARM can be particularly important for the validation of AMS as a tool to infer petrofabric, because it removes possible ambiguity in the interpretation related to inverse fabrics (e.g., switch between maximum and minimum principal axes due to the presence of magnetite single-domain (SD) particles) or composite fabrics (related to different coercivity of minerals) that can record distinct events during rock formation [e.g., *Stephenson et al.*, 1986; *Jackson et al.*, 1988; *Potter and Stephenson*, 1988; *Jackson*, 1991; *Trindade et al.*, 1999; *Borradaile and Gauthier*, 2003; *Potter*, 2004; *Raposo and Berquó*, 2008]. Both maximum principal axis and magnetic foliation have been used to infer magma flow, but there is still no consensus as to which is more reliable [e.g., *Borradaile and Gauthier*, 2006; *Callot et al.*, 2001; *Borradaile and Gauthier*, 2007]. The results from this study indicate that the angle between magnetic foliation and dyke wall is the more reliable indicator for magmatic flow.

2. Geological Setting and Sampling

2.1. General Setting

[5] The Foum Zguid dyke in southern Morocco is an extensive igneous intrusion, which is part of the Central Atlantic Magmatic Province (CAMP) one of the large igneous provinces on Earth [*Marzoli et al.*, 1999], related to the initial break-up of Pangaea [*May*, 1971]. The dominant normal polarity of the remanent magnetization found in these igneous rocks [*Hailwood and Mitchell*, 1971; *Hailwood*, 1975; *Martin et al.*, 1978; *Schott et al.*, 1981; *Smith*, 1987; *Knight et al.*, 2004; *Palencia-Ortas*, 2004; *Palencia-Ortas et al.*, 2006; *Silva et al.*, 2006a] indicates that these intrusions were most likely emplaced and cooled during a single polarity interval. Owing to the Jurassic reversal frequency in the magnetic polarity time scale [e.g., *Kent et al.*, 1995; *Nomade et al.*, 2000; *Besse and Courtillot*, 2002;], this suggests a short window of time for the intrusion of these rocks, which is in agreement with the radiometric dating [e.g., *Dunning and Hodych*, 1990; *Sebai et al.*, 1991; *Baksi and Archibald*, 1997; *Olsen et al.*, 2003; *Knight et al.*, 2004]. That argues for a short period of the CAMP formation over an area of approximately 7 million square kilometers, which represents a volume of basalts as large as that of Siberian or Deccan traps [*Olsen*, 1999]. The FZD was first dated at circa 189 Ma by K/Ar on whole rock [*Hailwood and Mitchell*, 1971], and later more precisely dated at 196.9 ± 1.8 Ma by $^{40}Ar/^{39}Ar$ [*Sebai et al.*, 1991].

[6] The FZD is vertical, NE-SW trending, and intrudes Precambrian and Paleozoic rocks of the Anti-Atlas belt in southern Morocco [*Hollard*, 1973; *Leblanc*, 1974]. The main igneous body of the FZD (Figures 1a and 1b), although segmented, can be followed for about 120 km showing an average thickness of approximately 120 m, accompanied by thinner (1–20 m thick), subparallel dykes contemporaneous of the main body [*Silva et al.*, 2006a, 2006b]. No evidence has been found in this or previous studies [e.g., *Marcais and Choubert*, 1956] for post-emplacement reactivation or deformation.

[7] According to *Aarab et al.* [1994], the tholeiitic magma of the FZD underwent a significant differentiation trend, leading to the presently observed gradual transition from dolerite at the margins to granophyre in the core.

[8] The host sedimentary rocks belong to the Adoudounian series, close to the southern limit of the Bou-Azzer El Graara window in the central Anti-Atlas Mountains [e.g., *Leblanc*, 1974]. They show variable degrees of contact metamorphism due to thermally induced recrystallization and Fe metasomatism [*Silva et al.*, 2006a, 2006b]. Newly formed hematite is the main product of this Fe metasomatism, and its amount reflects the metasomatic intensity experienced by the host sedimentary rocks. Therefore the metasomatism is more intense close to the thickest dyke and decreases with distance from dyke margins.

2.2. Structural Data

[9] Both dyke and host sedimentary rocks show a penetrative planar anisotropy close to the contact. Despite their geometrical similarity, the anisotropy appears to be different in igneous and sedimentary rocks. In the igneous rock it is defined by the alignment of minerals, most probably related to flow. In the sedimentary rock it is a mixture of fracturing and a spaced cleavage very close to dyke contact, and a fracture cleavage further away.

[10] The forceful intrusion of a thick dyke at depth must induce deformation in the host sedimentary rock. Two typical situations were found in the FZD: One where bedding is planar and orthogonal to dyke (stations FZ2, FZ7, FZ8, FZ11 and FZ12; see example at Figure 1c), and another where bedding is folded close to dyke contact (stations FZ1 and FZ9; Figure 1c). This difference in host rock response to compression is discussed later based on the magnetic data.

[11] From field observations and the image shown in Figures 1a and 2, the FZD appears as intruding an extensive fracture that does not show appreciable slip to make it a clear fault. Field observation and satellite image interpretation shows that: 1. The FZD is segmented, with local bifurcated terminations along the azimuths 8° or 65° (Figure 2a); 2. the FZD varies in strike, with variations commonly sharp as seen in Figure 2a and especially in Figure 2b (thinner dyke parallel to the FZD); 3. the northern sector of the FZD is characterized by vertical *en échelon*, sigmoidal, meter to decameter in thickness, quartz-filled veins that form impressive topographic highs (Figure 2c); 4. the quartz veins along around N-S (Figure 2c) or 60° in azimuth (Figure 2d), similar to the bifurcation of the main FZD, which indicates

Figure 2. Satellite images (available from Google) with geological interpretation of the northernmost segment of the dyke (station FZ12). Dotted ellipses mark quartzite ridges forming topographic highs; white rectangles mark areas zoomed in Figure 2b and 2d; solid black lines mark the FZD and secondary dyke; dashed black lines in Figure 2d mark the geometry of the quartz veins. Figure 2c is an area located to NE of Figure 2a, at coordinates 30°44′48.83″N, 6°09′23.63″W.


A
B
Foum Zguid Dyke
FZD
FZD
D
B
Dyke
1000 m
C
Foum Zguid Dyke
300 m
Google
D
Quartz ridge
Image © 2009 GeoEye
© 2009 Google
©2009 Google

Figure 2

that magma and silica-rich fluids filled similar fractures. The shape and arrangement of the quartz veins indicate a sinistral component of shear. This shear fracturing seems to be pre-intrusive to synintrusive, because the dyke cuts some veins, whereas other veins are curved into the dyke contact. Our interpretation is that the FZD magma intruded a crustal-scale shear fracture that, at this crustal level, allowed local opening as attested by the quartz-filled megaopen gashes. The deformation close to dyke has a trend different from the regional older deformation. The attitude of the planar discontinuities was measured at both margins, showing that such planes strike mainly subparallel to the dyke albeit they dip symmetrically and steeply towards the dyke (Figure 1d).

2.3. Sampling

[12] Oriented samples (450 in total) were collected along profiles perpendicular to the dyke wall at seven stations using a gasoline-powered portable drill. Of those, 322 samples were taken from the dyke itself and 128 from the host sedimentary rocks (from five of the seven stations (FZ1, FZ2, FZ8, FZ9 and FZ11); the letters "D" and "S" added to the site name indicate dyke or sediment, respectively). For two of the stations (FZ7 and FZ12), 30 samples from the dyke were also collected for rock magnetic and microscopic analyses. For the thin dykes (station FZ11) and for 2 of the other stations (FZ1 and FZ2), both margins were sampled. The contact between dyke and host rock was always visible and subvertical, and varied in azimuth between 34° and 70°. Each profile was several tens of meters long, and the distance from sample to the nearest contact was accurately measured. This sampling strategy allowed characterization of the magma flow from wall to core, and deformation of the host sedimentary rock to accommodate the forceful magmatic injection.

[13] Exceptions to the average dyke trend and thickness were found at two stations: 1. FZ2, where the igneous outcrops form two branches (120 and 20 m thick at sites FZ2D-A and FZ2D-B, respectively) separated by ~10 m of sediment; 2. FZ11, where two subparallel dykes, separated by ~31 m, bifurcate from a single dyke 50 m vertically below (the two are 2.3 m (dyke FZ11D-A) and 13.3 m (dyke FZ11D-B) thick.

[14] The sampled host rocks at stations FZ1 (sites FZ1S-A and B), FZ2 (sites FZ2S-A and FZ2S-B) and FZ8 (site FZ8S), comprise pelites and fine-grained quartzites. Similar to FZ8S [*Silva et al.*, 2006b], the host sediments at FZ1S-A, FZ2S-A and FZ2S-B record Fe metasomatism, which is deduced from petrographic observations with respect to hematite formation. The host rocks at FZ9S are carbonates, interbedded with volcano-sedimentary rocks. A bed of carbonates was selected for this study. The two main mineralogical features resulting from dyke intrusion observed in the carbonates are strong silicification and widespread hematite formation that occur mostly as aggregates (sometimes centimeter sized) or as small grains disseminated in the carbonate matrix. Submillimeter to millimeter thick veins of hematite together with crystalline carbonate and silica were also observed. These veins are either subparallel to bedding or strike parallel to the dyke margin (despite some variation in dip). The studied host rocks bordering the dyke at FZ11D-A (sites FZ11S-A/NW and FZ11S-A/SE on the NW and SE borders of the dyke) and FZ11D-B (FZ11S-B/NW and FZ11S-B/SE) are fine-grained quartzwackes and greywackes. More details about the sites are given in the appendix.

3. Methods

[15] AMS was used to assess the petrofabric, and the principal magnetic susceptibilities, $K_1 \geq K_2 \geq K_3$, were measured with a KLY3 Kappabridge. *Jelínek* [1981] parameters (corrected degree of anisotropy P' and shape parameter T) were used to characterize the magnetic fabric data. The orientation of the mean magnetic susceptibility ellipsoid and associated uncertainties was determined by the tensor variability statistics [*Hext*, 1963; *Jelínek*, 1978]. Magnetic zone axes with the associated confidence zones were determined by means of the bootstrap technique [*Henry*, 1997]. The AARM ellipsoid was acquired from 12 positions according to the design proposed by *Jelínek* [1993]. The statistical fit to the second-rank tensor was computed using AREF software (AGICO). Measurements were done with magnetometer JR6A after an acquisition of an anhysteretic magnetization with LDA-3A coupled with AMU-1A. The direct magnetic field had an intensity of 300 μT. Results for different coercivities were obtained for alternating magnetic fields (AF) of 10 or 20 mT (low field, LF) and 50 or 60 mT (high field, HF), which were chosen using the coercivity spectrum determined on our samples [*Jackson et al.*, 1988] after AF demagnetization at 100 mT. pAARM was determined from these measurements for low field ($pAARM_{LF\text{-}0\ mT}$), high field ($pAARM_{HF\text{-}LF\ mT}$), and the whole range ($pAARM_{HF\text{-}0\ mT}$) of coercivities, with AARM axes here defined as $P_1 \geq P_2 \geq P_3$.

[16] Thermomagnetic $K(T)$ measurements were made in argon-controlled atmosphere until a maximum temperature of 700°C, for a total of 40 samples, using a CS3 furnace coupled with KLY3 Kappabridge. Curie temperatures were determined using the inverse magnetic susceptibility methodology according to the Curie-Weiss law [*Petrovský and Kapička*, 2006]. For high-field experiments, a laboratory made translation inductometer within an electromagnet was used. Classical hysteresis parameters were determined after paramagnetic correction. The coercivity spectrum was evaluated by the acquisition of pARM due to an application of a low direct field (300 μT) for 5 mT AF windows [*Jackson et al.*, 1988].

[17] Scanning Electron Microscopic (SEM) observations and Energy Dispersive Spectra (EDS) analysis were performed on carbon-coated rock fragments cut from igneous and sedimentary rocks. Analyses were done using a Jeol JSM-6360LV microscope and a Noran Instrument EDS analyzer, enabling the identification of the mineral composition, while Secondary Electron Imaging (SEI) was used to determine morphology and textural relationships. In order to estimate the depth of intrusion, chemical analyses were carried out on amphibole using a JEOL JXA-8500F microprobe, operating at 15 kV and 10 nA, with a beam diameter of 5 μm.

4. Microscopy Analyses

4.1. Petrography

[18] The properties and distribution of magnetic carriers in the igneous rock, which are typically less than 3% of rock

volume, are strongly dependent on location within the dyke, and can be correlated with the distinct textures and silicate mineral association observed along dyke cross sections. Igneous textures of samples collected at less than 2 m from the margins typically have a fine-grained subophitic texture (chilled margin) with plagioclase laths enclosing anhedral to subhedral grains of clinopyroxene, orthopyroxene, serpentinized olivine, magnetite, ilmenite, and accessory biotite. Small (<15 μm), disseminated grains of chalcopyrite are frequent, and pyrite is rarer (Figure 3a). These samples can also display porphyritic textures with euhedral to subhedral olivine (frequently replaced by serpentine or iddingsite), orthopyroxene and clinopyroxene phenocrysts immersed in a microcrystalline matrix of plagioclase, pyroxene, olivine, magnetite, and lesser modal amounts of ilmenite and biotite. Weak amount of secondary magnetite occurs associated with pyroxene and olivine oxidation and hydration (Figure 3b). Primary textures from these samples attest to fast cooling and crystallization of magma (chilled margin) in the contact with sedimentary host rocks, which is in contrast with the coarse phaneritic textures found in samples collected at distances greater than ~2 m from the dyke walls. The phaneritic samples are characterized by a mesoscopic igneous banding, displaying a primary mineral association dominated by euhedral to subhedral plagioclase, clinopyroxene, Ti-magnetite (and possibly chromite), relatively scarce olivine, horneblende, accessory biotite and granophyre intergrowths of feldspar and quartz. Magnetite grains can reach 1 mm in diameter and are often characterized by the presence of thick ilmenite sandwich laths (Figure 3c). The hydrothermal effects related to later stages of magma cooling (temperatures <400°C) are noticeable in these rocks, being progressively represented by the uralitization of pyroxene and, as a consequence, the development of horneblende by hydrolysis of plagioclase with the appearance of sericite, oxidation of primary magnetite and ilmenite lamellae formation (Figure 3d), further development of maghemite on magnetite (Figures 3d–3f), and partial replacement of biotite and horneblende by chlorite. The occurrence of skeletal ilmenite in close association with horneblende is also common (Figure 3g). The host sedimentary rocks close to dyke contact underwent metasomatic transformations induced by the FZD intrusion, which are dominated by hematite formation [*Silva et al.*, 2006a, 2006b].

[19] Chemical data obtained on primary hornblende crystals (Table 1) from the more differentiated rocks emplaced at the dyke's core allowed the application of the geobarometer calibrated by *Schmidt* [1992] based on hornblende Al content (precision of ±0.6 kbar). Assuming a density average of 2700 kg/m^3 for the continental crust, calculated pressure data correlates to intrusion depths between 8 and 11 km.

4.2. SEM Observations

[20] Dolerite samples, collected at distances <2 m from the FZD margins, typically show high concentration of small euhedral Ti-iron oxides (~20 μm), without visible exsolution textures, (Figures 4a–4d), confirming the observations with reflected light petrographic microscope. Such features point to rapid cooling and argue for the primary origin of the magnetic mineralogy of the dyke along their margins. Samples located ~2 m from the contact start to exhibit higher concentration in large Ti-iron oxides (titanomagnetite, >50–100 μm). Iron oxides are present either as well-preserved prismatic crystals (<50 μm, titanomagnetite; Figure 4f) or as larger corroded lamellar semi-hexagonal minerals (>100 μm, titanohaematite; Figure 4h). Epigenetic pyrite is locally found filling fractures (Figure 4g). The magnetic mineralogy of samples located ~5 m from the contact comprises coarser Ti-iron oxides(>200 μm; Figures 4i and 4j) and rare chalcopyrite in contact with titanomagnetite (Figure 4k).

[21] Sedimentary rocks far from the dyke contact (>30 m away) are characterized by ubiquitous fenestral porosity (20–50 μm in diameter) and by an absence of primary Ti-iron oxides (Figures 5a and 5d). Most bright minerals observed with backscattered electron images correspond to zircon, plagioclase and paramagnetic iron-bearing minerals such as biotite (Figures 5a, 5e, and 5f), while iron oxides are mostly represented by very fine, spherical, secondary hematite (<10 μm, pigment) (Figures 5b, 5c, and 5d). Larger botryoidal iron oxides (>400 μm) are found filling voids and fenestral porosity. The magnetic mineralogy of sediments from near the contact with the dyke differs significantly from that of samples far from the contact. Fenestral porosity is absent or hardly distinguishable (Figure 5g). Monazite, identified by P, La, and Ce peaks on EDS spectra, together with barite are ubiquitous (Figures 5g and 5i). The origin of sulfur is most likely in the dolerite. A detrital origin for monazite is suggested, while barite could precipitate in the water column (i.e., marine barite), in supersaturated pore fluids (diagenetic barite) or come from hydrothermalism. Iron is present as severely altered iron-bearing minerals (relic of magnetite?) and hematite pigments (Figures 5h and 5j). Ti-iron oxides are also found in the form of rutile (TiO_2) and titanomagnetite (Figures 5k and 5l). A primary origin for the titanomagnetite in Figure 5l is however questionable since the well-preserved euhedral morphology of the crystal is contradictory with the detrital character of the sedimentary rocks. The magnetic mineralogy observed in the sediments suggests a secondary origin for most iron oxides.

5. Rock Magnetism

[22] Magnetic methods were applied to determine the main ferromagnetic carriers and their physical properties along cross sections. Samples from host sediments were the object of a previous detailed rock magnetic study [*Silva et al*. 2006b]. *Silva et al*. [2004] showed in a preliminary study of the FZD that there is no significant variation in the mineralogical composition of the magnetic carriers in the FZD, though important textural differences were recognized (i.e., size, shape and distribution of the rock forming

Figure 3. Typical textural arrangements resulting from high-temperature exsolution and/or metasomatic processes. Samples from sites (a, b) FZ7-NW2/B; (c, d, e, g) FZ2A-SE/C; (f) FZ1-NW/B. Clinopyroxene, chlpy; maghemite, mgh; magnetite, mgt; ilmenite, ilm; olivine, olv; serpentine, spt. See section 4.1 text for details.

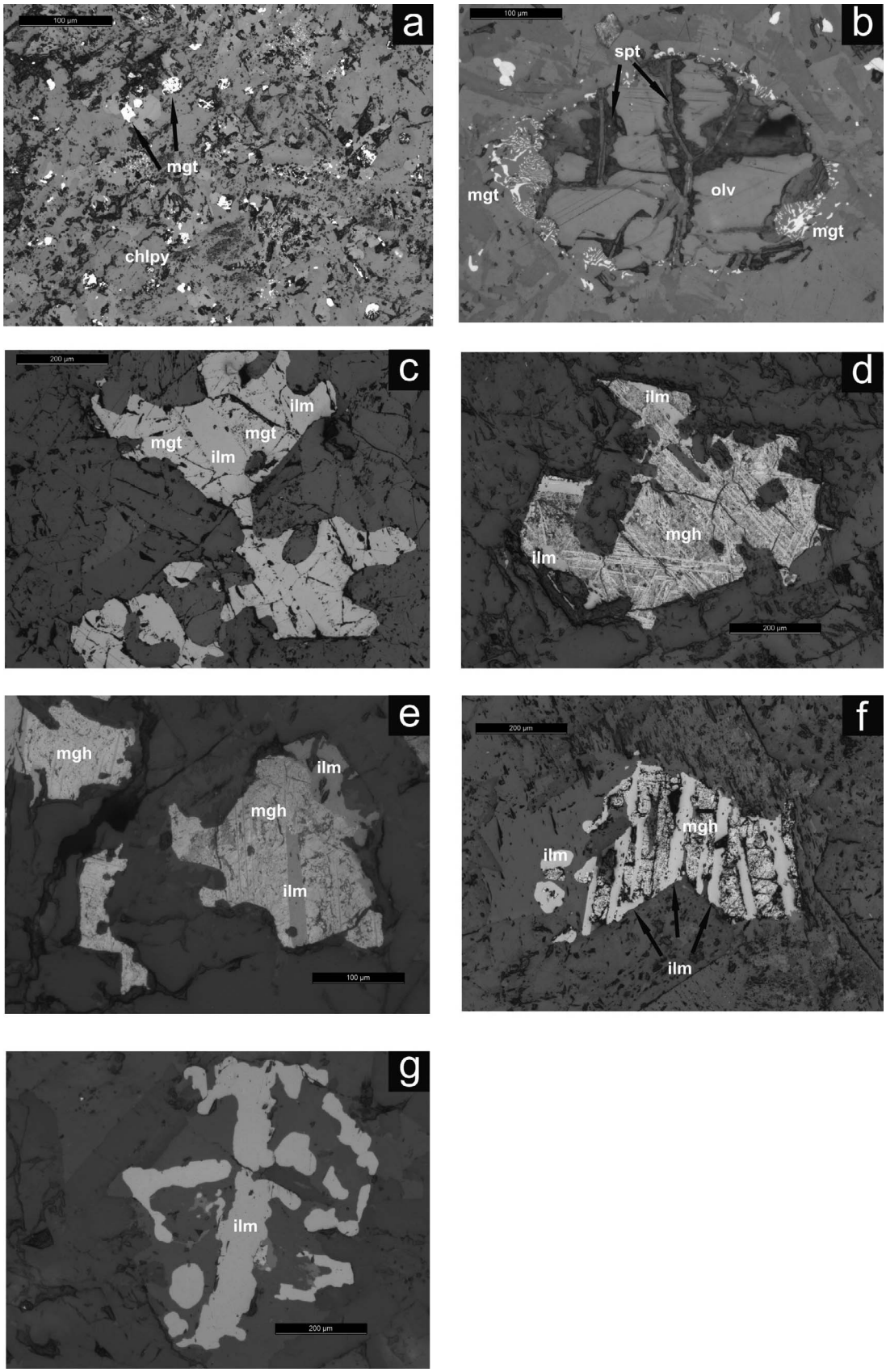
a
100 µm
mgt
chlpy
b
100 µm
spt
mgt
olv
mgt
c
200 µm
ilm
mgt
mgt
ilm
d
ilm
mgh
ilm
200 µm
e
mgh
ilm
mgh
ilm
100 µm
f
200 µm
mgh
ilm
ilm
g
ilm
200 µm

Figure 3

Table 1. Representative Hornblende Chemical Analyses From Samples Emplaced at the Core of the Foum Zguid Dyke

Horneblende	Core	Core	Rim	Rim
SiO_2	43.44	44.57	44.32	44.49
TiO_2	1.42	1.57	1.71	1.41
Al_2O_3	6.78	6.21	6.40	5.88
FeO	26.46	24.87	25.52	25.50
MnO	0.35	0.27	0.26	0.25
MgO	6.15	6.90	6.96	6.63
CaO	10.31	9.86	9.70	9.38
Na_2O	1.96	1.85	1.99	1.96
K_2O	0.85	0.77	0.08	–
F	0.73	0.85	0.61	0.70
Total	98.45	97.73	97.56	96.20
Al tot[a]	1.250	1.138	1.172	1.089

[a]The Al total was calculated following *Schumacher* [1997].

minerals, which can be ascribed to cooling processes). Ti-low titanomagnetite with a dominant pseudosingle domain state was determined as the main magnetic carrier. We present here more extensive and detailed magnetic analyses on more samples and sites to better constrain the origin of the magnetic fabric.

5.1. Thermomagnetic Measurements

[23] Most thermomagnetic experiments yielded reversible cycles (see example of samples FZ7 in Figure 6a) with Curie temperatures ranging between 490° and 570°C (Figure 6b). This temperature range indicates Ti-poor titanomagnetite as the main magnetic carrier [e.g., *O'Reilly*, 1984; *Dunlop and Özdemir*, 1997; *Lattard et al.*, 2006], as expected for the doleritic nature of the analyzed rocks and supported by the microscopic observations.

[24] However, some samples revealed reversibility only for temperatures lower than 300°–400°C, a temperature for which an irreversible hump in K intensity was observed (see example of samples from stations FZ2 and FZ11 in Figure 6a). The cooling run of such samples shows $K(T)$ values rather lower than those observed during the heating run. This irreversible behavior probably denotes an inversion of a meta-stable magnetic phase, such as maghemite, to another magnetic phase with lower K, most likely hematite [*Dunlop and Özdemir*, 1997]. The slight steplike character observed for sample FZ11 during the final and fast drop of $K(T)$ values and the small hump observed for temperatures around 350°–400°C could also indicate the presence of a slight oxidation of titanomagnetite, probably due to maghemitization, as verified from microscopic analyses.

5.2. High-Field Measurements

[25] High-field measurements reveal simple hysteresis loops typical of a single magnetic phase with low coercivity (Figures 6c and 6d). Such results reinforce the interpretation of Ti-low titanomagnetite as the main magnetic carrier [*Lowrie*, 1990, and references therein]. The Day plot [*Day et al.*, 1977] was used to infer the titanomagnetite grain type, with the standard boxes for single-domain (SD), pseudo-single-domain (PSD) and multi-domain (MD), as redefined by *Dunlop* [2002]. The majority of data is bracketed between PSD and PSD/SD transition domains (Figure 6e), closely following the trend of SD + MD mixture curves [*Dunlop*, 2002], with coercivity ratio values mostly between 1.8 and 3.5 (Figure 6f). This suggests a mixture of these two end members. For some samples, in particular from sites with undefined AMS fabrics (see below), a shift to the right could be due to the presence of accessory minerals like maghemite and hematite, in addition to the main magnetic carrier, titanomagnetite.

[26] The coercivity spectrum obtained by pARM acquisition curves (Figure 6g) closely agrees with the results obtained from hysteresis cycles. According to *Jackson et al.* [1988] the occurrence of the main peak on the curve for applied fields lower than 20 mT is due to a ferrimagnetic population coarser than 3 μm. For the curve that shows a decrease of pARM intensity since the lowest applied fields, grain size of 25 μm or larger is expected for the coarser grains. For fields higher than 20 mT, the shape of pARM curves suggests the presence of finer ferrimagnetic grains that can have a size around 1.0 μm or even be smaller than 0.1 μm (SD population).

6. Rock Magnetic Properties Along Cross Sections

[27] The bulk magnetic properties show the variable character of the dyke along cross sections. With increasing distance to dyke wall, variations of the values of saturation magnetization (J_s) and susceptibility (K) occur gradually, or in the form of an abrupt transition, or as a sequence of plateaux (Figure 7). Changes of the coercive ratio are related with dyke thickness and distance to the wall. The thinner dykes at FZ11 show a slight increase of this parameter with the distance to the margin, while for thicker segments the opposite relation is observed (compare the thickness of hysteresis cycles obtained for the margin and core in Figures 6c and 6d). Lower values of this parameter are observed for inner domains of the thicker segments of the dyke (Figure 6f). The coercivity spectrum obtained by pARM also points to an increase of the coercivity towards the core of the main dyke due to a decrease of size of the coarser population (shift of the peaks to higher applied fields) and to an increase of the amount of the thinner population relative to the coarser (Figure 6g).

[28] The obtained Curie temperatures spectra can be divided into subranges according to the thickness of the dyke; the thinner the dyke, the lower the average Curie temperature (Figure 6b). At FZ11, composed of two sub-parallel branches of the same intrusion, Tc ranges between 490 and 500°C for the thinner dyke (FZ11A with 2.3 m) and from 520° to 535°C for the thicker one (FZ11B with 13.3 m). For all the remaining stations, located along the main igneous body (typically presenting a thickness around 100–140 m), Tc values vary between 540° and 570°C, with the lowest values obtained for domains nearest the margins.

7. Magnetic Fabric

7.1. Dyke

[29] Samples nearest the margins mostly show, within each site, similar anisotropy ellipsoids, which can be prolate or oblate depending on site (see examples for prolate shape in Figures 7d and 7f, and for oblate shape in Figures 7a and 7c); therefore, sites are internally consistent in terms of the AMS ellipsoid. In contrast, samples located farther from the

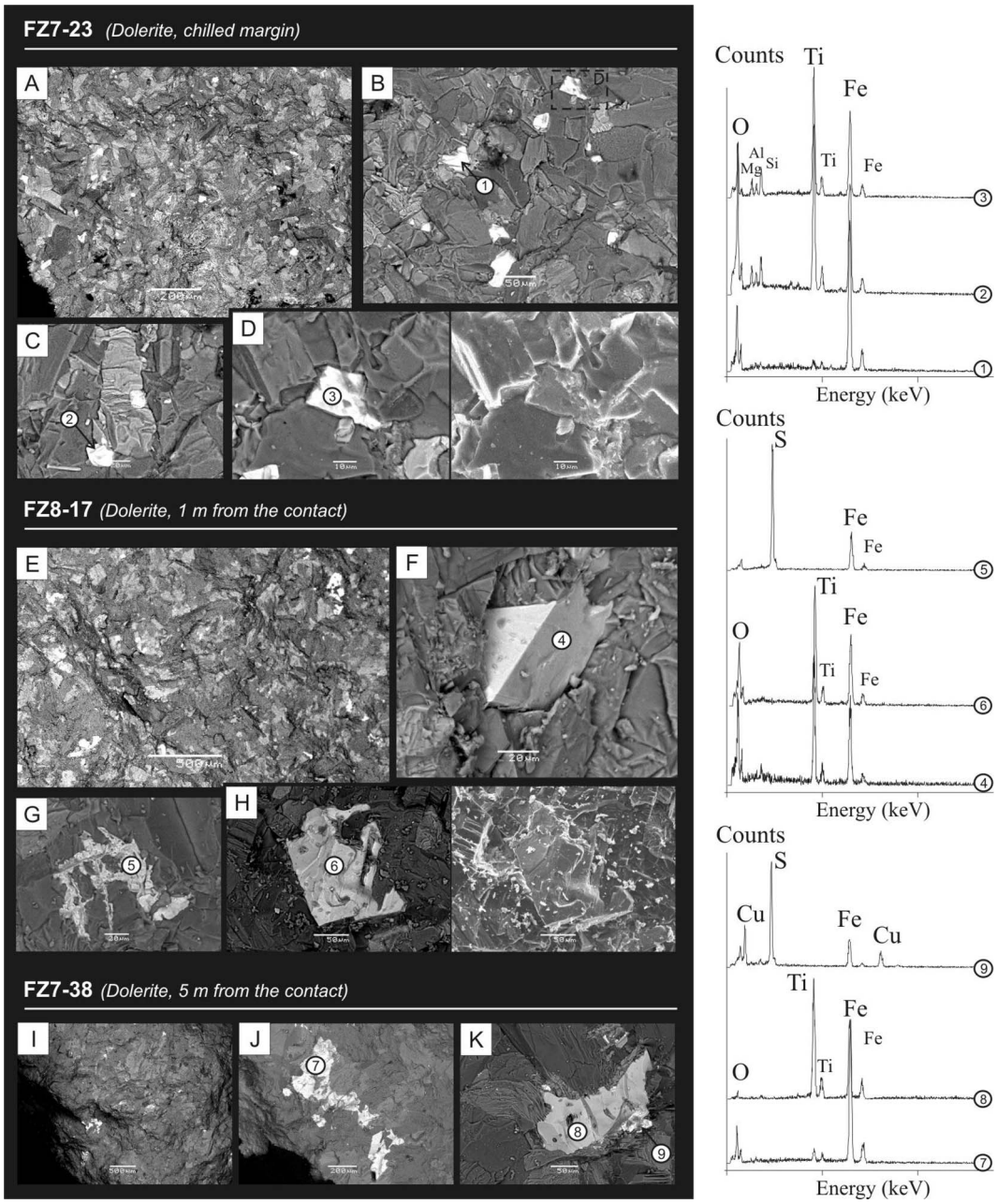

Figure 4. Scanning electron microscopy (SEM) and energy dispersive spectra (EDS) analysis of FZD dolerite (see section 4.2 for details).

margins are inconsistent because they show prolate and oblate ellipsoids within the same site (Table 2 and T versus distance diagrams in Figure 7). Samples nearest the margin with a well-marked oblate ellipsoid show a magnetic foliation dipping towards the core of the dyke and K_1 well clustered and plunging subparallel to foliation dip (except for FZ12D). Samples nearest the margin with a prolate ellipsoid show K_3 somewhat scattered along a plane perpendicular to K_1, defining a magnetic zone axis subparallel to K_1 (see Table 2).

[30] Further away from the margins, an increase in orientation dispersion of each principal axis is observed (see FZ1D-SE/C, FZ2DA-SE/C, FZ7D-NW/D, FZ8D-SE/D, and FZ9D-NW/D at Figure 7). Despite some dispersion, FZ7, FZ8, and FZ9 still show reasonable internal consistency and are therefore used to infer petrofabric. Otherwise, despite the results obtained for each sample of sites FZ1D-SE/C and FZ2DA-SE are statistically significant, the variation obtained from sample to sample lead to a random fabric that cannot be used to deduce petrofabric.

[31] Stereoplots comprising all data from each station show appreciable dispersion of the principal axes, because dispersion increases and orientation varies with distance to dyke wall. Concerning P', the values are relatively low (mostly <1.05) and, despite some few sites nearest the margins where there seems to be some correlation with K (see variation of K and of P' for station FZ1 on Figure 7a), there is no systematic variation of P' with K (Figure 7).

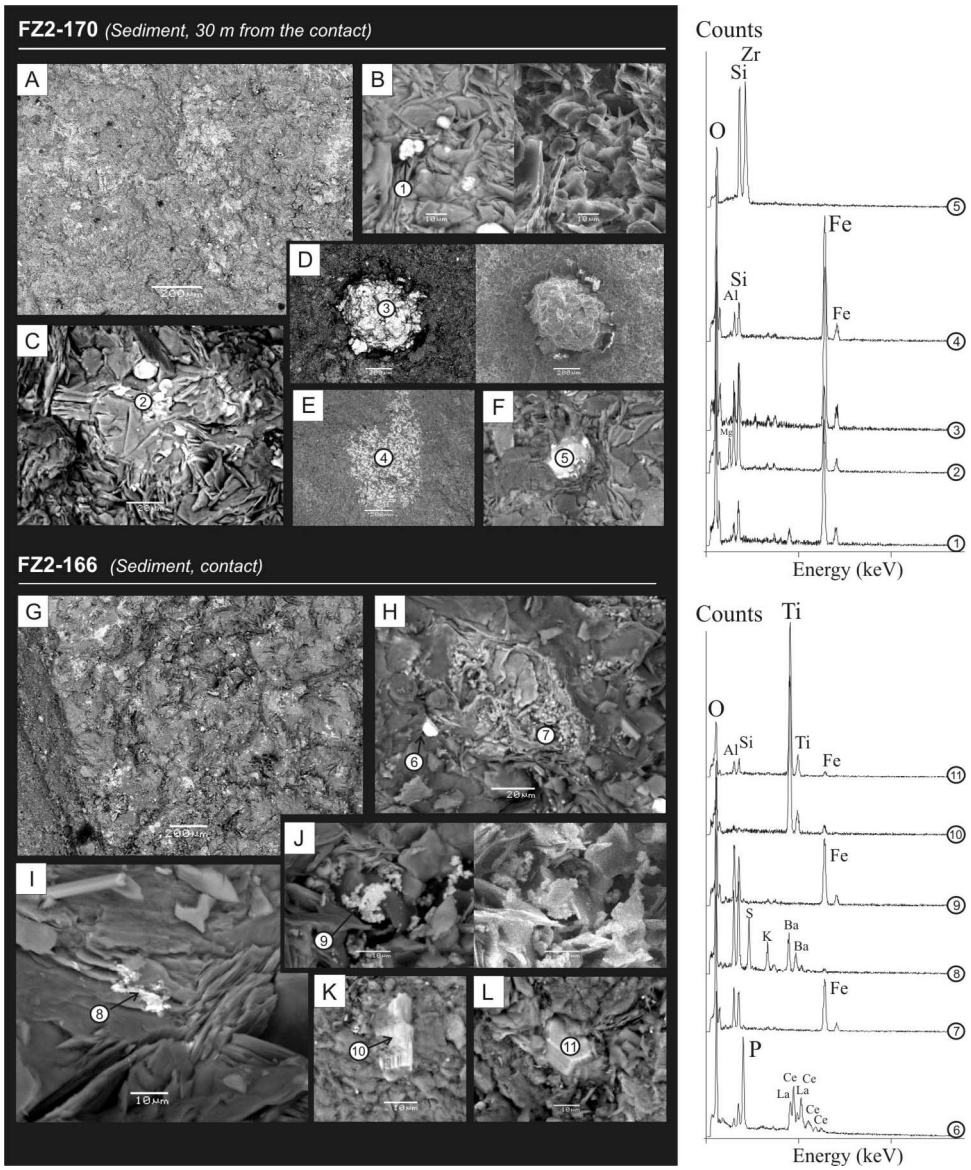

Figure 5. Scanning electron microscopy (SEM) and energy dispersive spectra (EDS) analysis of FZD sedimentary host rocks (see section 4.2 for details).

[32] Based on orientation and shape of the AMS ellipsoid, and on magnetic zone axis orientation, it is possible to classify the samples into three types of magnetic fabric ([*Silva et al.*, 2008]; see Table 2). Magnetic fabric 1 is characterized by prolate AMS ellipsoids and well defined zone axis coincident with K_1 (Figure 8a). Fabric 2 is characterized by AMS ellipsoids whose shape varies from oblate to prolate and by poorly defined zone axis (Figure 8b). Fabric 3 corresponds to oblate ellipsoids and undefined magnetic zone axes (Figure 8c); the strikes of magnetic foliation and dyke are similar, but dips are different. Fabric 2 occurs at sites further away from the margins, and fabrics 1 and 3 at sites the nearest to the margins (mostly within chilled margins).

[33] Sixty seven samples corresponding to different types of AMS fabric were submitted to pAARM measurements to better constrain the meaning of the AMS fabric in terms of petrofabric. Examples of results for each type are presented in Figure 9. Comparison of the AMS and pAARM fabrics for some individual samples and for the mean fabrics of 4–6 samples from the same site indicate: 1. For AMS Fabric 1 (Figure 9a), the orientations of AMS and pAARM ellipsoids

Figure 6. Rock magnetism results for dolerite. (a) Thermomagnetic behavior of dolerite samples performed under Argon-controlled atmosphere; (b) evolution of the Curie temperatures along the cross sections; typical hysteresis loops from stations (c) FZ7 and (d) FZ12; (e) *Day et al*. [1977] diagram with limits and mixing curves proposed by *Dunlop* [2002]; (f) evolution of the coercivity ratio along the cross sections; and (g) remanent coercivity spectrum obtained from pAARM with an AF window of 5 mT and direct field of 0.3 mT. Values are normalized by the highest value.

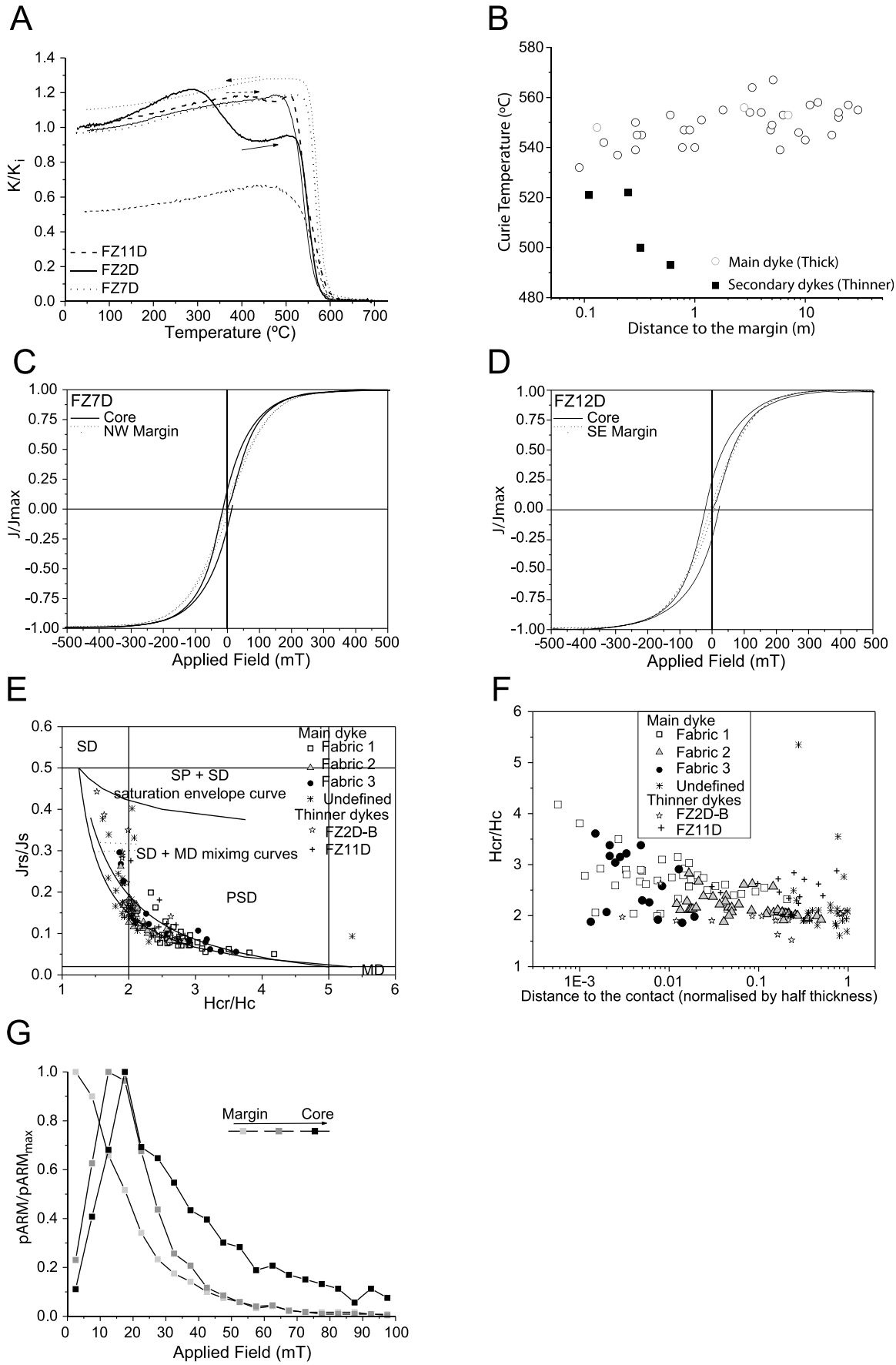
A
K/K$_i$
Temperature (ºC)
FZ11D
FZ2D
FZ7D
B
Curie Temperature (ºC)
Distance to the margin (m)
Main dyke (Thick)
Secondary dykes (Thinner)
C
FZ7D
Core
NW Margin
J/Jmax
Applied Field (mT)
D
FZ12D
Core
SE Margin
J/Jmax
Applied Field (mT)
E
SD
SP + SD
saturation envelope curve
SD + MD mixing curves
PSD
MD
Main dyke
Fabric 1
Fabric 2
Fabric 3
Undefined
Thinner dykes
FZ2D-B
FZ11D
Jrs/Js
Hcr/Hc
F
Main dyke
Fabric 1
Fabric 2
Fabric 3
Undefined
Thinner dykes
FZ2D-B
FZ11D
Hcr/Hc
Distance to the contact (normalised by half thickness)
G
Margin
Core
pARM/pARM$_{max}$
Applied Field (mT)

Figure 6

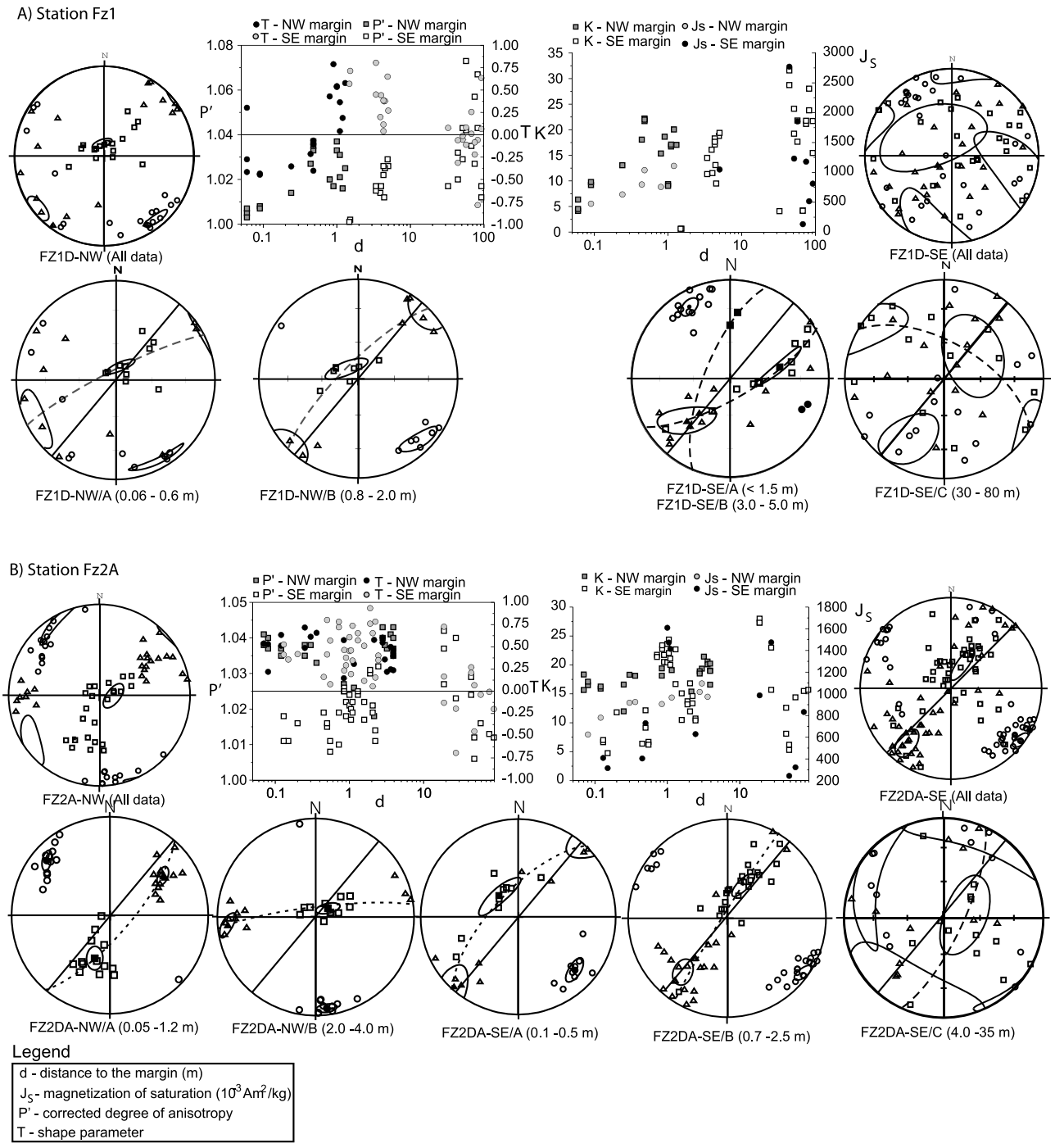

Figure 7. For each station are presented equal area stereographic projections (lower hemisphere) with indication of the maximum K_1 (squares), intermediate K_2 (triangles) and minimum K_3 (circles) magnetic susceptibility principal axes; evolution of the following parameters with the distance to the contacts: P', corrected degree of anisotropy; T, shape parameter; K, bulk magnetic susceptibility; and Js, magnetization of saturation. Figures 7a to 7f correspond to the main dyke and Figure 7g corresponds to the thinner dykes.

are different and the magnetic fabrics are sometimes not coincident for different grain sizes because pAARM axes for the high coercivity (smaller grains) are closer to the AMS axes than for lower coercivity (bigger grains) (e.g., sample FZ1D-34, Figure 9a). For site FZ12D-B a permutation of the principal axes between AMS fabric and the pAARM fabrics is observed and the pAARM magnetic foliations are almost perpendicular to the dyke plane. 2. For AMS Fabric 2, (Figure 9b), K_3 and P_3 are well clustered and share the direction of the dyke pole. Significant variations occur for P_1, which can be related to the shape of AMS ellipsoids. When the AMS ellipsoid is prolate, P_1 and K_1

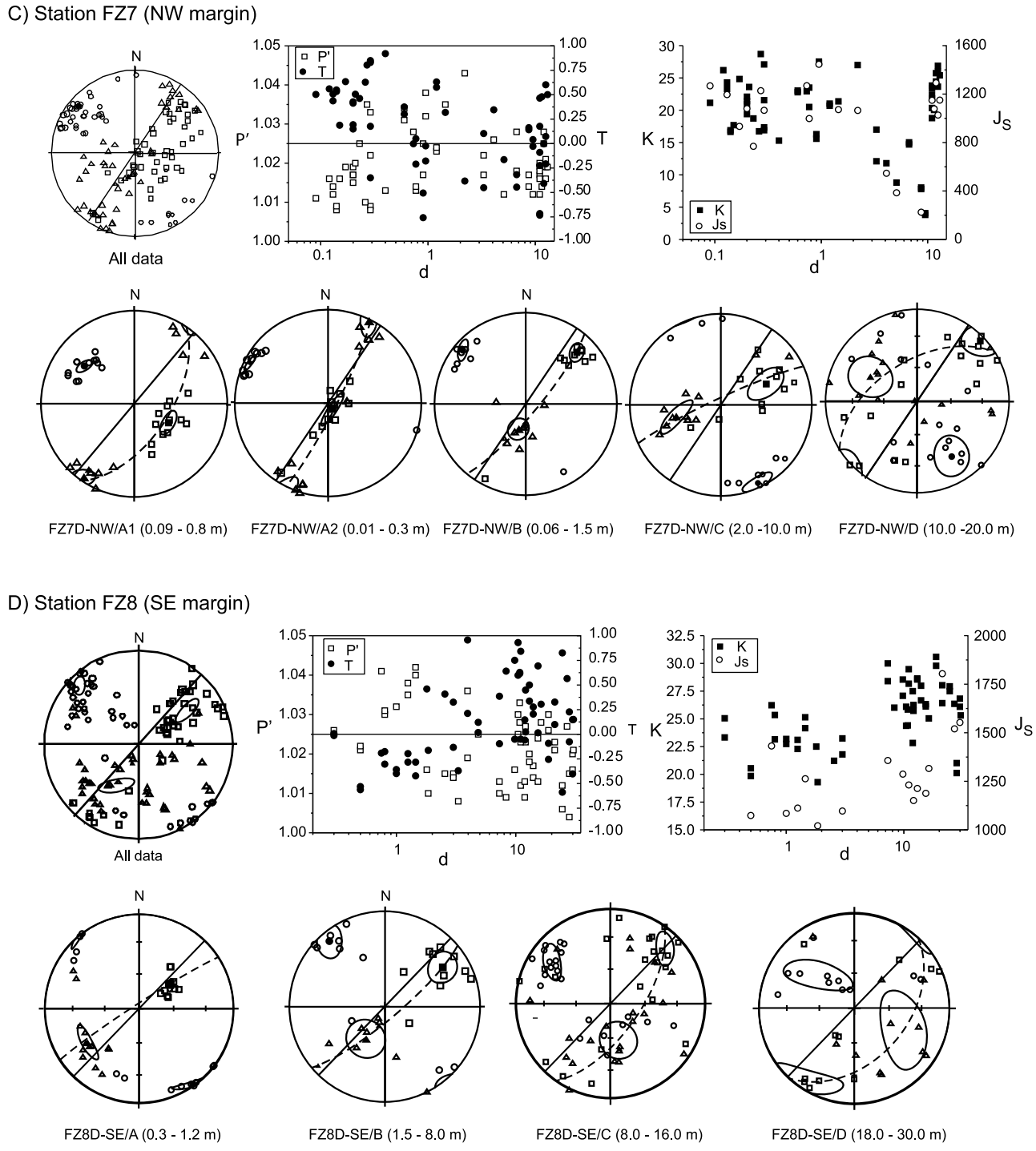

Figure 7. (continued)

share the same subhorizontal direction; when the ellipsoid is oblate, P_1 is mostly subvertical; when the ellipsoid is neutral, two distinct components are sometimes identified according to the coercivity spectrum. A low-field coercivity component ($pAARM_{LF\text{-}0\ mT}$) is associated with a P_1 plunging subvertically, while a high-field coercivity component ($pAARM_{HF\text{-}LF\ mT}$) shows P_1 with the orientation of K_1, and both plunging at very low angle (nicely illustrated by samples from site FZ7D-NW2/B, Figure 9b). This indicates a control of the fabric by the coercivity, hence grain size. 3. For AMS Fabric 3, the different examples display similar orientations of the remanence and susceptibility ellipsoids (Figure 9c). The transition from fabric 3 to fabric 1 is associated with the more prolate AMS ellipsoids, and corresponds to the development of a composite magnetic fabric.

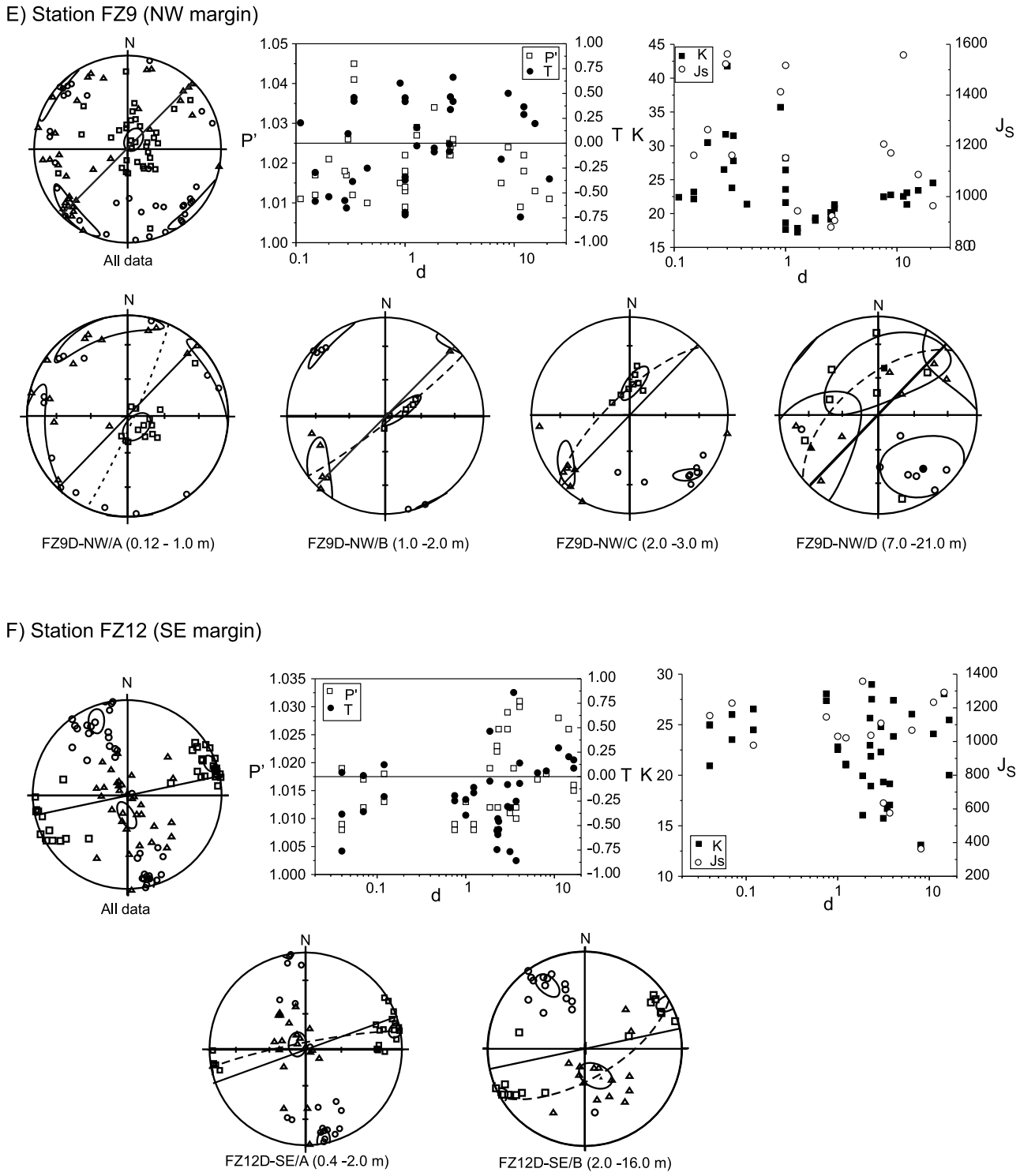

Figure 7. (continued)

7.2. Host Sedimentary Rocks

[34] The K, T, P' values and the orientation of the magnetic susceptibility ellipsoid show significant variations along cross sections, in most cases related to dyke thickness and distance to dyke wall (Figure 10). Sites FZ1S-B, FZ2S-A and B, and FZ11S-B/SE and NW show a gradual increase in K towards the contact, FZ8S shows an opposite correlation, and the SE margin of the thinner dyke at FZ11S-A shows similar values of K all along the profile. The carbonates of site FZ9S show a large spread in K values (2–3 orders of magnitude) with no obvious correlation with distance to the contact. These results point to the presence of a strong heterogeneity in the concentration of magnetic carriers as observed microscopically and mesoscopically.

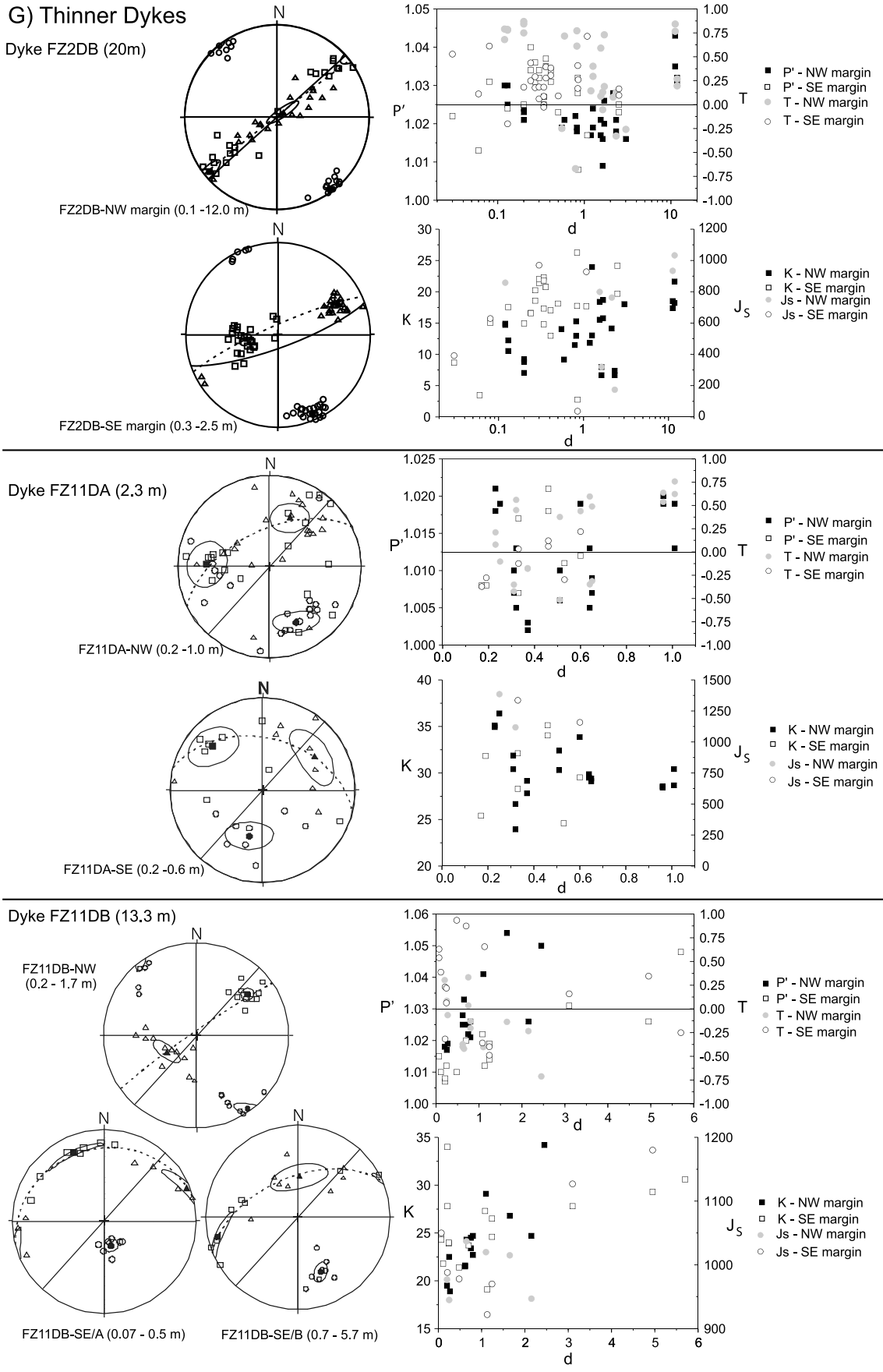

Figure 7. (continued)

Table 2. Magnetic Properties of Sampled Sites[a]

Sites	D/margin (m)	Dyke (Az°/dip°)	N	K ± SD	K_1 (D°/I°)	K_3 (D°/I°)	P'	T	ZA^1 (D°/I°)	ZA^2 (D°/I°)	α (°)	β (°)	Fabric
Station FZ1													
FZ1D-NW/A	0.06–0.6/NW	40/90	10	13.1 ± 7.3	18/78	153/8	1.016	−0.34	46/66		24	23	1
FZ1D-NW/B	0.8–2.0/NW	40/90	12	15.4 ± 4.1	312/77	135/13	1.023	0.45		28/50	14	5	2
FZ1D-SE/A	< 1.5/SE	40/90	2	0.7 ± 0.1	3/40	112/21	1.002	0.64			27	18	3
FZ1D-SE/B	3.0–5.0/SE	40/90	11	14.3 ± 5.4	92/59	330/17	1.018	0.64		76/41	26	20	2
FZ1D-SE/C	30–80/SE	40/90	14	19.1 ± 8.8	305/9	210/30	1.019	−0.10		334/45	81	80	×
Station FZ2													
FZ2D/B-NW	0.1–12.0/NW	48/90	21	13.6 ± 4.7	236/18	144/4	1.021	0.66		237/6	7	6	2
FZ2D/B-SE	0.3–2.5/SE	70/78	25	17.3 ± 5.5	259/59	155/8	1.026	0.25		60/38	21	5	3
FZ2D/A-NW/A	0.05–1.2/NW	40/90	13	17.0 ± 1.9	158/51	309/17	1.032	0.58		55/41	17	1	3
FZ2D/A-NW/B	2.0–4.0/NW	40/90	11	19.0 ± 1.7	55/76	174/7	1.036	0.43		353/83	44	44	2
FZ2D/A-SE/A	0.1–0.5/SE	40/90	9	7.9 ± 2.6	314/68	134/22	1.013	0.53		265/60	22	4	3
FZ2D/A-SE/B	0.7–2.5/SE	40/90	18	18.0 ± 4.7	26/59	126/6	1.020	0.54		28/48	7	4	2
FZ2D/A-SE/C	4.0–35/SE	40/90	12	16.6 ± 8.2	84/71	295/16	1.011	−0.24		124/74	22	15	×
Station FZ7													
FZ7D-NW1/A	0.09–0.80/NW	34/90	12	19.3 ± 2.8	113/57	306/33	1.027	0.11		174/46	33	2	3
FZ7D-NW2/A	0.12–0.30/NW	34/90	11	23.1 ± 3.7	125/83	299/7	1.020	0.67		189/69	9	5	3
FZ7D-NW2/B	0.6–1.5/NW	34/90	10	21.9 ± 3.9	45/22	310/12	1.027	0.11		50/42	13	6	2
FZ7D-NW2/C	2.0–10.0/NW	34/90	11	11.8 ± 6.6	65/42	155/1	1.016	0.06		263/76	31	31	2
FZ7D-NW2/D	10.0–20.0/NW	34/90	16	22.6 ± 2.8	51/11	148/36	1.011	0.03		243/8	42	24	2
Station FZ8													
FZ8D-SE/A	0.3–1.2/SE	44/90	13	23.4 ± 1.8	52/56	147/4	1.030	−0.44	51/58		14	13	1
FZ8D-SE/B	1.5–5.0/SE	44/90	10	24.3 ± 4.1	58/21	323/12	1.015	0.19		52/14	15	9	2
FZ8D-SE/C	7.0–16.0/SE	44/90	22	26.8 ± 1.8	45/19	305/25	1.011	0.11		40/15	27	9	2
FZ8D-SE/D	18.0–30.0/SE	44/90	11	26.4 ± 3.2	212/10	312/46	1.013	−0.02		185/30	46	2	2
Station FZ9													
FZ9D-NW/A	0.12–1.0/NW	44/90	14	28.1 ± 5.8	138/79	254/5	1.015	−0.04	112/79		21	20	1
FZ9D-NW/B	1.0–2.2/NW	44/90	6	18.6 ± 1.0	71/75	322/5	1.027	−0.02		62/70	9	8	2
FZ9D-NW/C	1.0–2.4/NW	44/90	8	21.0 ± 1.1	8/63	136/17	1.017	0.04		22/52	17	2	2
FZ9D-NW/D	7.0–21.0/NW	44/90	7	22.9 ± 1.0	7/50	140/30	1.009	0.47		28/37	31	6	2
Station FZ11													
FZ11D/A-NW	0.23–1.01/NW	42/90	20	30.3 ± 3.0	335/55	150/35	1.006	0.67		20/48	39	18	2
FZ11D/A-SE	0.19–0.60/SE	42/90	8	30.1 ± 3.9	312/30	192/41	1.009	0.06		349/40	68	60	2
FZ11D/B-NW	0.20–1.65/NW	42/90	12	24.2 ± 3.9	51/29	143/3	1.025	−0.28	53/27		11	11	1
FZ11D/B-SE/A	0.07–0.50/SE	42/90	7	25.2 ± 4.0	340/21	164/69	1.011	0.51		331/22	72	32	2
FZ11D/B-SE/B	0.70–5.70/SE	42/90	8	26.1 ± 3.6	252/6	158/35	1.023	0.59		266/22	43	26	2
Station FZ12													
FZ12D-SE/A	0.4–2.0/SE	70/90	21	23.7 ± 3.6	78/6	169/6	1.011	−0.42	78/1		11	9	1
FZ12D-SE/B	2.0–16.0/SE	70/90	14	23.0 ± 4.8	61/5	329/25	1.020	0.01	232/15		27	11	1

[a]D/margin, distance in meters of the samples to the nearest dyke margin; Dyke, mean azimuth (Az) and dip degrees of the dyke wall following the right-hand rule) N, number of samples; K ± sd, bulk magnetic susceptibility ± standard deviation; K_1, mean declination (D) and inclination (I) of the maximum susceptibility axis; P', average values of corrected degree of anisotropy; T, average values of shape parameter of the magnetic susceptibility ellipsoid; ZA^1, well clustered zone axis; ZA^2, poorly defined zone axis; α, angle between magnetic foliation and dyke plane; β, angular difference in azimuth between K_3 and pole of the dyke; Fabric, type of identified AMS fabric; ×, undefined AMS fabric.

[35] In cross sections where the sedimentary strata are planar and orthogonal to the dyke (FZ2S and FZ8S), there is a progressive change in ellipsoid shape and axes orientation when approaching the dyke contact; from a flat fabric within the bedding plane, to a prolate fabric with K_1 horizontal (marking the intersection of bedding and dyke plane), then to an oblate fabric parallel to the dyke plane, and even to a slightly more prolate fabric with steeper K_1 parallel to the dyke plane very close to the contact. K_3 follows a great circle subperpendicular to the dyke trend. A similar evolution is observed for stations where bedding is folded near the contact (stations FZ1S-B and FZ9S).

[36] Host rocks bordering thinner apophyses of the FZD show a different behavior. Samples from the NW margin of the thinner dyke FZ2S-B show, along the whole cross section, a similar orientation of the principal axes of the magnetic susceptibility ellipsoid, defining a subhorizontal magnetic foliation with a magnetic lineation mostly subparallel to dyke direction (Figure 10). Host rock samples bordering dyke FZ11D-B show relatively scattered orientations of the principal axes of the magnetic ellipsoid for samples farther away from the dyke; closer to the dyke, the magnetic foliation becomes parallel to bedding. Samples from host sediments bordering the thinner dyke FZ11D-A show a magnetic foliation subparallel to bedding for samples located at the NW margin, while samples from the section across the SE margin present a poorly defined magnetic fabric.

[37] The shape changes are accompanied by variations in the P' values as: 1. A regular decrease at FZ1S-B and FZ2S-A and B; 2. a regular increase for samples bordering the two margins of dyke FZ11B; and 3. no coherent variations for FZ9S. Samples from FZ8S mainly show similar T and P' values along the cross sections, while for FZ11S-A/SE and FZ11S-A/NW, T and P' show variations not related with distance to the contact.

[38] Far away from the contact (~400 m, site FZ1S-A) the sedimentary beds are only affected by the earlier regional deformation, comprising mostly open folds with hinges plunging 10° towards azimuth 118° (Figure 10a). Here

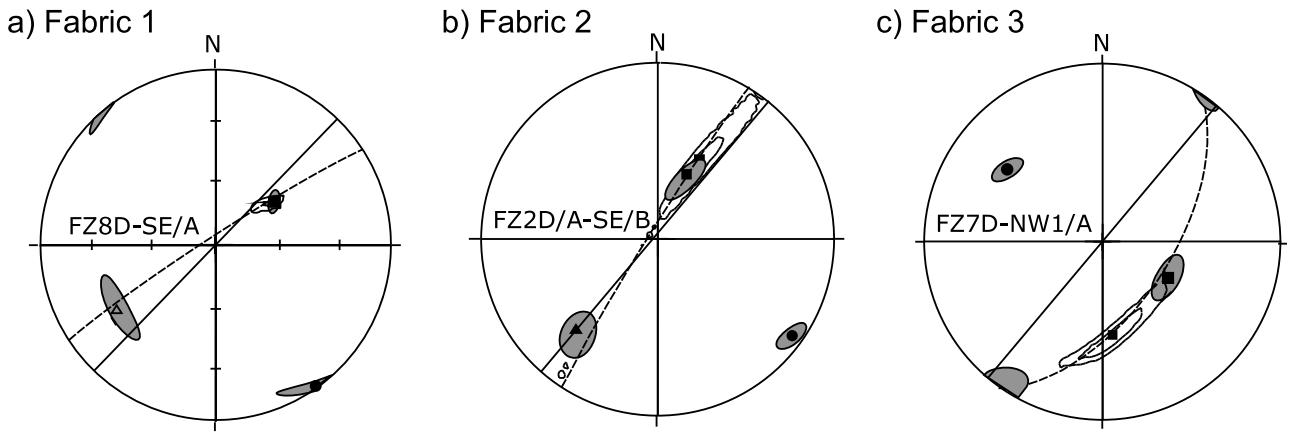

Figure 8. Equal area stereographic projections (lower hemisphere) exemplifying typical behaviors of zone axis confidence ellipses: (a) For fabric 1 (example of the site FZ8D-SE/A); (b) fabric 2 (example FZ2DA-SE/B), and (c) fabric 3 (example FZ7D-NW1/A). Dashed line represents the magnetic foliation plane. Confidence zones at 95% and 63% from 10,000 bootstrap resampling. Confidence zones of magnetic susceptibility principal axes correspond to shaded areas. Squares, triangles, and circles corresponding to the maximum K_1, intermediate K_2, and minimum K_3 principal axes, respectively, of the magnetic susceptibility ellipsoid.

K values are low and constant. The susceptibility ellipsoid is mainly oblate for a degree of anisotropy ranging from 1.005 to 1.018. K_3 is subperpendicular to bedding, even in fold limbs.

8. Discussion

8.1. Dyke

8.1.1. Dyke Cooling and Origin of Composite Fabrics

[39] Towards the core of thicker segments of the dyke we found: 1. An increase in Curie temperature; 2. a decrease of the coercivity ratio; 3. peaks of pARM gradually evolving toward AF higher intensities; 4. variations of the magnetic parameters sensitive to the concentration of ferromagnetic minerals (K and Js), which can occur gradually as abrupt transitions or as a sequence of plateaux; 5. variations of the shape of the AMS ellipsoid (T), from oblate or prolate to a nondefined shape; and 6. variations of orientation and clustering of AMS principal axes. All these data indicate that the crystallization of ferromagnetic carriers during the cooling of the dyke underwent textural and mineralogical transformations mainly due to metasomatic and oxidation-exsolution processes.

[40] High-temperature exsolution lamellae processes responsible for the mixture of magnetite-ilmenite in pre-existing Ti-spinels grains promoted an enrichment of low-Ti titanomagnetite towards the core of the dyke. This explains the gradual increase of Curie temperatures towards inner domains of the dyke. The coercivity ratio and pARM spectrum, magnetic parameters that are correlated with the magnetic grain size [*Day et al.*, 1977; *Jackson et al.*, 1988; *Dunlop*, 2002], indicate that the amount of small magnetite grains increases towards the core of the dyke, where coarser grains can be observed but where oxidation-exsolution of ferromagnetic carriers and metasomatic processes acted more intensely. Solid-state diffusion of Fe and Ti during the oxidation-exsolution process can effectively decrease the size of the magnetic carrier [e.g., *Wilson et al.*, 1968; *Ade-Hall et al.*, 1971]. If the size of magnetite lamellae is sufficiently small (reaching SD behaviors), a component with inverse fabric [*Stephenson et al.*, 1986; *Potter and Stephenson*, 1988; *Rochette*, 1988] can start to contribute to the resulting AMS fabric. Depending on the relative proportion between a mixture of SD and MD grains the resulting AMS fabric frequently reflects a fabric not related to the mineral orientation distribution [*Rochette et al.*, 1999; *Ferré*, 2002].

[41] From the evaluation of the coercivity ratio according to the type of fabric and distance to the contact (compare Figures 6d and 6e), we verify that fabrics achieved at the chilled margins (fabrics 1 and 3) show values mostly ranging between 2 and 4, fabrics achieved for inner domains (undefined fabrics) between 1.5 and 2.5, and for intermediate distances (fabric 2) between 1.8 and 3. The oxidation-exsolution complex structures, which occur more intensely at inner parts of the dyke, could be the explanation for the presence of composite fabrics of type 2 and the two sites with undefined fabrics (see Table 2), with resultant shape variation and inconsistency of the AMS fabric in some sites. Similar results were obtained for an equivalent dolerite dyke in Iberia (Messejana-Plasencia dyke, MPD). *Silva et al.* [2008] reported that inverse fabrics [*Stephenson et al.*, 1986; *Potter and Stephenson*, 1988; *Rochette*, 1988], responsible for a significant amount of "abnormal" fabrics, seemed to be related to exsolution processes that led to an overall effective decrease of the Ti-spinel grain size

Figure 9. Equal area stereographic projections (lower hemisphere) illustrating AMS and AARM principal axes for each type of AMS fabric. Stereographic projections on the shaded area correspond to sites (with N indicating the number of samples), while the remaining projections are examples of individual samples.

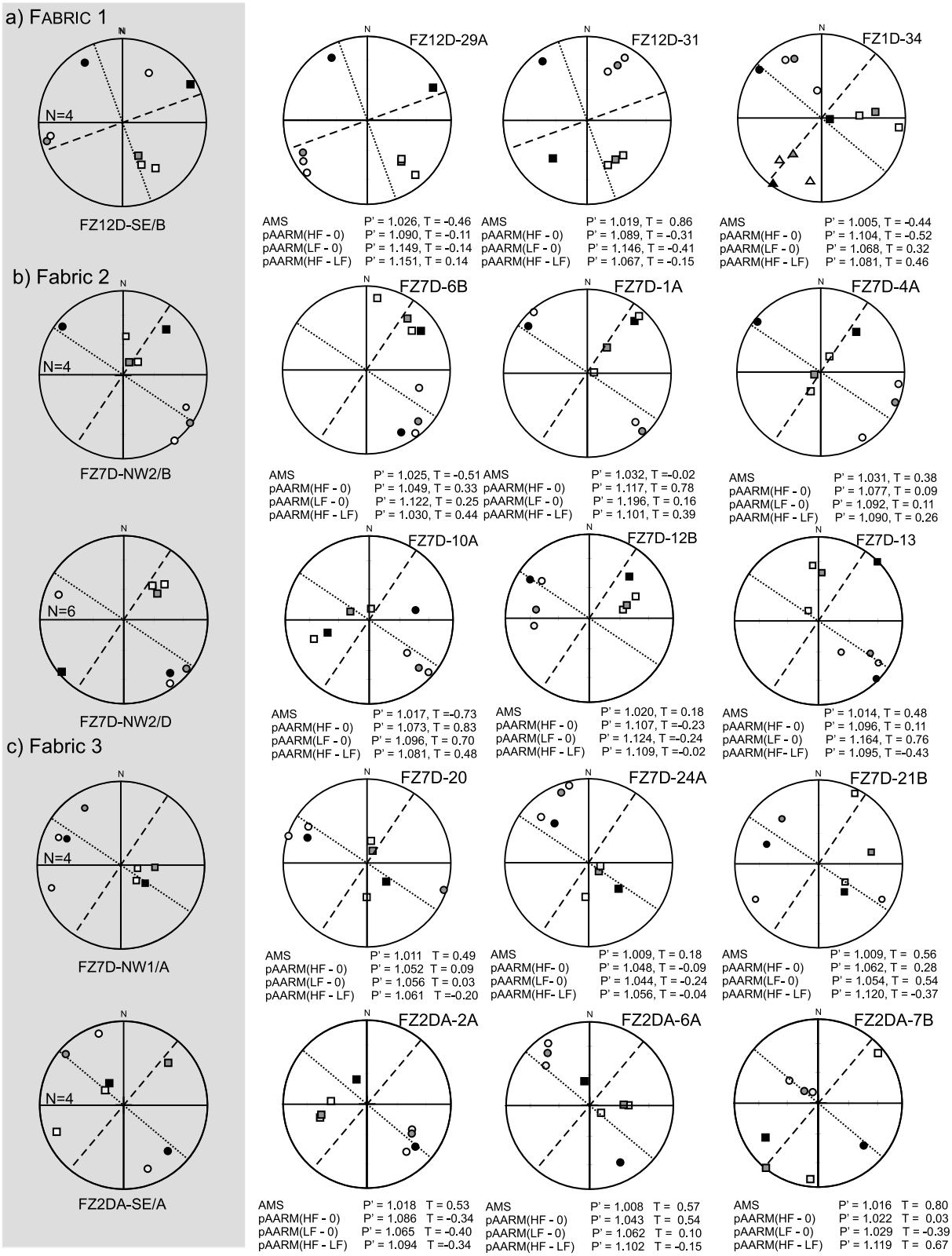
a) Fabric 1
N=4
FZ12D-SE/B
b) Fabric 2
N=4
FZ7D-NW2/B
N=6
FZ7D-NW2/D
c) Fabric 3
N=4
FZ7D-NW1/A
N=4
FZ2DA-SE/A
FZ12D-29A
AMS P' = 1.026, T = -0.46
pAARM(HF - 0) P' = 1.090, T = -0.11
pAARM(LF - 0) P' = 1.149, T = -0.14
pAARM(HF - LF) P' = 1.151, T = 0.14
FZ12D-31
AMS P' = 1.019, T = 0.86
pAARM(HF - 0) P' = 1.089, T = -0.31
pAARM(LF - 0) P' = 1.146, T = -0.41
pAARM(HF - LF) P' = 1.067, T = -0.15
FZ1D-34
AMS P' = 1.005, T = -0.44
pAARM(HF - 0) P' = 1.104, T = -0.52
pAARM(LF - 0) P' = 1.068, T = 0.32
pAARM(HF - LF) P' = 1.081, T = 0.46
FZ7D-6B
AMS P' = 1.025, T = -0.51
pAARM(HF - 0) P' = 1.049, T = 0.33
pAARM(LF - 0) P' = 1.122, T = 0.25
pAARM(HF - LF) P' = 1.030, T = 0.44
FZ7D-1A
AMS P' = 1.032, T =-0.02
pAARM(HF - 0) P' = 1.117, T = 0.78
pAARM(LF - 0) P' = 1.196, T = 0.16
pAARM(HF - LF) P' = 1.101, T = 0.39
FZ7D-4A
AMS P' = 1.031, T = 0.38
pAARM(HF - 0) P' = 1.077, T = 0.09
pAARM(LF - 0) P' = 1.092, T = 0.11
pAARM(HF - LF) P' = 1.090, T = 0.26
FZ7D-10A
AMS P' = 1.017, T =-0.73
pAARM(HF - 0) P' = 1.073, T = 0.83
pAARM(LF - 0) P' = 1.096, T = 0.70
pAARM(HF - LF) P' = 1.081, T = 0.48
FZ7D-12B
AMS P' = 1.020, T = 0.18
pAARM(HF - 0) P' = 1.107, T =-0.23
pAARM(LF - 0) P' = 1.124, T =-0.24
pAARM(HF - LF) P' = 1.109, T =-0.02
FZ7D-13
AMS P' = 1.014, T = 0.48
pAARM(HF - 0) P' = 1.096, T = 0.11
pAARM(LF - 0) P' = 1.164, T = 0.76
pAARM(HF- LF) P' = 1.095, T =-0.43
FZ7D-20
AMS P' = 1.011 T = 0.49
pAARM(HF - 0) P' = 1.052 T = 0.09
pAARM(LF - 0) P' = 1.056 T = 0.03
pAARM(HF - LF) P' = 1.061 T =-0.20
FZ7D-24A
AMS P' = 1.009, T = 0.18
pAARM(HF- 0) P' = 1.048, T = -0.09
pAARM(LF- 0) P' = 1.044, T = -0.24
pAARM(HF- LF) P' = 1.056, T = -0.04
FZ7D-21B
AMS P' = 1.009, T = 0.56
pAARM(HF - 0) P' = 1.062, T = 0.28
pAARM(LF- 0) P' = 1.054, T = 0.54
pAARM(HF - LF) P' = 1.120, T = -0.37
FZ2DA-2A
AMS P' = 1.018 T = 0.53
pAARM(HF - 0) P' = 1.086 T = -0.34
pAARM(LF - 0) P' = 1.065 T = -0.40
pAARM(HF - LF) P' = 1.094 T =-0.34
FZ2DA-6A
AMS P' = 1.008 T = 0.57
pAARM(HF - 0) P' = 1.043 T = 0.54
pAARM(LF - 0) P' = 1.062 T = 0.10
pAARM(HF - LF) P' = 1.102 T = -0.15
FZ2DA-7B
AMS P' = 1.016 T = 0.80
pAARM(HF - 0) P' = 1.022 T = 0.03
pAARM(LF - 0) P' = 1.029 T = -0.39
pAARM(HF - LF) P' = 1.119 T = 0.67
Legend
AMS
K1
K3
pAARM (LF - 0 mT) P1 P3
pAARM (HF - 0 mT) P1 P3
pAARM (HF - LF mT) P1 P3
LF - Low field (10 to 20 mT)
HF - High field (50to 60 mT)
Perpendicular to dyke plane
Dyke plane

Figure 9

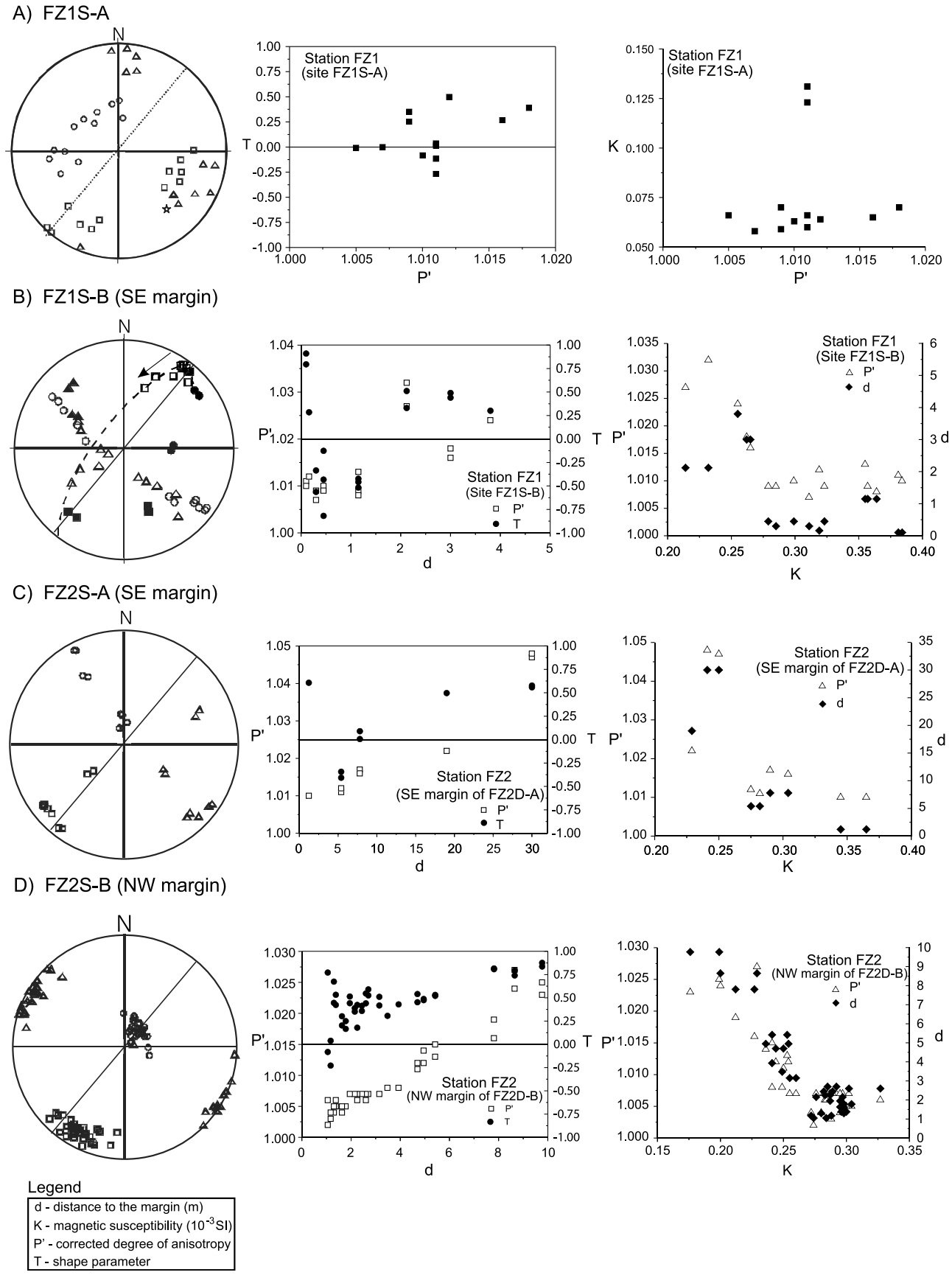
A) FZ1S-A
N
Station FZ1
(site FZ1S-A)
T
P'
Station FZ1
(site FZ1S-A)
K
P'
B) FZ1S-B (SE margin)
N
Station FZ1
(Site FZ1S-B)
P'
T
d
Station FZ1
(Site FZ1S-B)
P'
d
T P'
K
C) FZ2S-A (SE margin)
N
Station FZ2
(SE margin of FZ2D-A)
P'
T
d
Station FZ2
(SE margin of FZ2D-A)
P'
d
T P'
K
D) FZ2S-B (NW margin)
N
Station FZ2
(NW margin of FZ2D-B)
P'
T
d
Station FZ2
(NW margin of FZ2D-B)
P'
d
T P'
K
Legend
d - distance to the margin (m)
K - magnetic susceptibility (10-3SI)
P' - corrected degree of anisotropy
T - shape parameter

Figure 10

(SD grains). However, coercivity ratio values of the FZD are mostly between 1.8 and 4, while for MPD mostly between 1.5 and 3.2, indicating that, although present, oxidation-exsolution and metasomatic processes underwent by the FZD were not as intense as for the MPD (a result compatible with the microscopic analysis). Metasomatic processes, mainly hydration and hydrolysis, coeval with the later cooling stages of the dyke, were responsible for the formation of maghemitic fringes and for the presence of secondary fine-grained ferromagnetic mineral aggregates from hydrous-phyllosilicates. Therefore, such processes can also contribute to the presence of composite fabrics with consequences for the inconsistency of the AMS fabric in some sites [*Henry and Meurisse*, 1978].

8.1.2. Magnetic Fabrics

[42] Scattering of the AMS principal axes is observed in stereoplots containing all data from each station (Figure 7). However, when AMS is analyzed site by site along each station profile, clustering of axes improves significantly, which means that the fabric orientation depends on distance to dyke margin. A similar behavior has been observed by several authors [e.g., *Baer*, 1995, *Hrouda et al.*, 2002; *Féménias et al.*, 2004; *Silva et al.*, 2008; *Cañón-Tapia and Herrero-Bervera*, 2009]. The AMS fabric mostly shows well-clustered ellipsoids that define a magnetic foliation with angular deviations from the dyke plane below 30° (see α in Table 2). Such a fabric has been assumed as potential indicator of magma flow under simple shear. However, the comparison with the pAARM fabric in the present study revealed the presence of composite AMS fabrics for a significant number of sites. This clearly shows that special caution is needed regarding the use of our AMS results as a potential tool to infer magma flow.

[43] For Fabric 3, the good agreement between the principal directions of AMS and pAARM ellipsoids indicates the absence of significant composite fabrics. The AMS fabric is then not related to the coercivity of the ferromagnetic minerals.

[44] For Fabric 2, the comparison between AMS and pAARM suggests the presence of two fabrics related to different coercivities. P_3 and K_3 share an orientation similar to the pole of the dyke, but P_1 shows a subvertical plunge for a low coercivity component (coarse grains), and a subhorizontal plunge (as K_1) for a high coercivity component (small grains). These results reveal that the use of K_1 as a marker for preferential mineral alignment for fabrics of type 2 can be erroneous. K_3 and P_3 mark the pole of the magnetic foliation. The presence of poorly constrained AMS fabrics of type 2 for sites far from the margin can be explained by high-temperature oxidation-exsolution and/or later hydrothermal transformations, as microscopically observed. Another possibility can be related with a flow that departs from simple shear.

[45] Fabric 1 presents significant differences between AMS and pAARM ellipsoids: 1. Contrary to most pAARM fabrics, AMS ellipsoids are prolate; 2. K_3 shows a girdle distribution, while P_3 mostly shares the direction of the dyke pole; and 3. K_1, which is not coincident with P_1, has the orientation of the magnetic zone axis. These results clearly show that the ferrimagnetic fabric is not related with a single preferential orientation, but has a heterogeneous character that seems to result from the competition between subfabrics. While a permutation between axes is clearly observed at FZ12D-B (which suggests the presence of an inverse fabric due to SD magnetite), the same is not observed for sites nearest the margin with this type of fabric (example of sample FZ1D-34 in Figure 9a). Domains nearest the margins underwent changes of the stress field during the initial stages of the opening and propagation of the dyke tip, which could give rise to complex strain regimes promoting the appearance of subfabrics not necessarily aligned (further discussion below in section 8.3). Therefore, magnetic fabric 1, which is composite, likely has two distinct origins.

[46] Only fabrics 2 and 3 have been then selected to interpret the petrofabrics. For fabric 3, the use of K_1 or the imbrication between magnetic foliation and dyke plane to infer magma flow lead to similar results. For fabric 2, as indicated above, only imbrication can be used. Both types of AMS fabric indicate a steeply to subvertical magma flow.

[47] Fabric 1 and partially fabric 2 show strong evidence of the presence of composite fabrics. Similar results were recently observed for other dolerite dykes such as the great MPD in Iberia [*Silva et al.*, 2008] and Cuaró Mesozoic dyke swarm in Uruguay [*Masquelin et al.*, 2009]. As verified by this work, and previously proposed by *Chadima et al*. [2009], complementary measurements of AARM or pAARM fabrics could give important clues regarding the identification of composite fabrics and so help in the characterization of the petrofabric.

8.2. Deformation of Host Sedimentary Rocks

[48] As verified by *Silva et al.* [2006a, 2006b] for FZD host rocks, variations in K may result from chemical changes in mineralogy during the intrusive process. The thicker the dyke and the closer the samples are to the contact, the more intense are the mineralogical and textural transformations due to a thermally induced recrystallization and Fe-metasomatism experienced by the host sedimentary rocks.

[49] There is a major difference between the AMS fabrics observed along cross sections through sediments hosting thin and thick dykes: The magnetic foliation is parallel to bedding close to thin dykes and parallel to the dyke close to thick dykes. Therefore there was no appreciable deformation (mostly flattening but also folding) mechanically imposed by the thin intrusions (i.e., magnetic ellipsoid orientation

Figure 10. Evolution of the magnetic fabric in the sedimentary host rocks along cross sections perpendicular to the dyke. Equal area stereograph projections (lower hemisphere) with indication of (a) the K_1 (squares), K_2 (triangles), and K_3 (circles) AMS principal axes; dashed line indicating the trend of the dyke plane; arrow indicating the evolution of a principal axes with the approach to the dyke. (b–h) Remaining graphics show the evolution of K (bulk magnetic susceptibility), P' (corrected degree of anisotropy), and T (shape parameter), along the cross sections. Data from sites FZ8S and FZ11S were adapted from *Silva et al*. [2006a, 2006b].

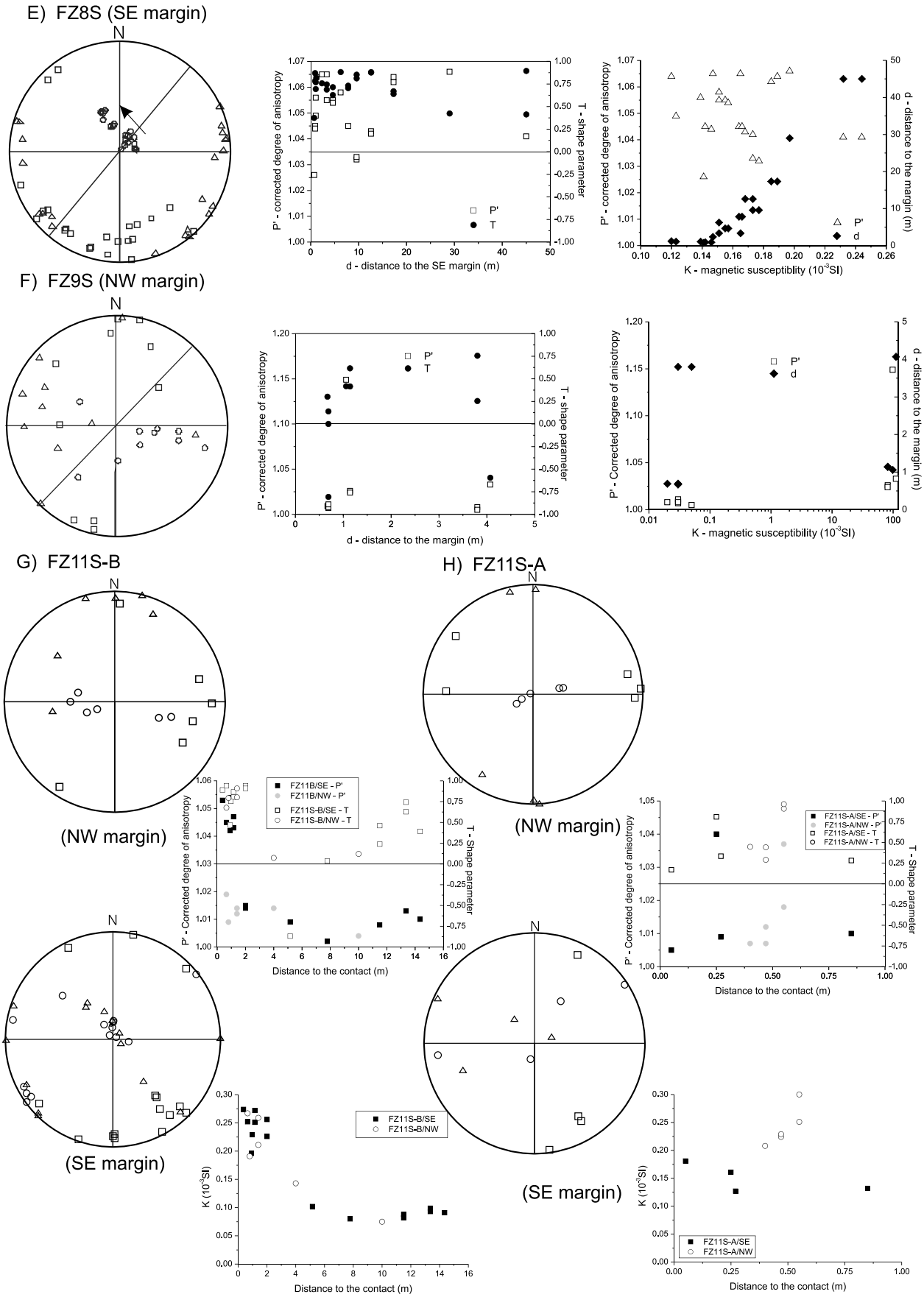

Figure 10. (continued)

remained unchanged, in contrast to the folding and flattening associated with thick dyke forceful injection). The dyke-parallel magnetic foliation near the contact with thick segments of the FZD shows that deformation imposed by the thick and hot intrusion on the host rock had a great effect in the development of the magnetic foliation; otherwise this foliation would be parallel to bedding as in the thin dykes where temperature dominated over deformation.

[50] A purely thermal (alteration of preexisting minerals) or mimetic (growth of minerals in the preexisting structure, the bedding plane) mechanism cannot explain the formation of this new magnetic fabric with foliation parallel to the dyke, because this foliation is independent of the initial sedimentary fabric. Such an evolution is very similar to the effect of a progressive deformation of sediments due to a compression direction within the bedding plane [e.g., *Aubourg et al.*, 1999]. Dehydration due to heating should also have induced volume loss, which helped in finding room for magma injection. The SEM analysis revealed the vanishing of fenestral porosity for samples nearest the contact, an indication that such rocks were compacted during the intrusive process. The evolution of the magnetic fabric toward the dyke margin corroborates the presence of flattening; that is, the progressive evolution from a purely sedimentary fabric, first to the development of an intersection lineation with decrease of the global anisotropy and increase of the prolateness, and finally to the occurrence of a foliation plane perpendicular to bedding with progressive increase of the global anisotropy and flattening.

[51] Near the contact with thicker segments of the dyke, the results obtained for the host rocks record, in addition to thermal and chemical alterations [*Silva et al.*, 2006a, 2006b], mechanical effects of magma forceful injection responsible for the accumulation of damage in the host rocks [*Lyakhovsky et al.*, 1997; *Mériaux et al.*, 1999]. The magnetic fabric studies of sedimentary host rocks show that the emplacement of this dyke was accompanied by important thermal, mechanical and chemical effects. The host rocks close to dyke were flattened and/or folded to make room to magma intrusion. The upward deflection of bedding closest to dyke indicates an upward movement of the magma.

8.3. Flow and Emplacement

[52] *Knight and Walker* [1988] observed a good agreement between K_1 orientation and independent mesoscopic flow-related structures from Hawaiian dykes, and proposed the use of K_1 as an indicator of magma flow. However, this has proven to be inappropriate under certain circumstances [e.g., *Baer* 1995; *Callot and Guichet*, 2003; *Chadima et al.*, 2009; *Silva et al.*, 2008]. For instance, K_1 can represent an intersection lineation (subparallel to the magnetic zone axis as defined by *Henry*, 1997) due to the superposition of planar and flow-related subfabrics, therefore showing significant angular deviations from the true magma flow. Assuming the stability of the magnetic foliation under the superposition of subfabrics, *Geoffroy et al.* [2002] proposed the use of imbrication between magnetic foliation and dyke plane as a reliable tool to determine flow sense.

[53] Under a simple shear regime, microstructural [e.g., *Blanchard et al.*, 1979; *Blumenfeld and Bouchez*, 1988; *Correa-Gomes et al.*, 2001] and AMS studies have shown that mineral shape preferred orientations commonly make an angle up to 30° with the dyke wall. When this angle is greater than 30°, the fabric has been called "abnormal" [e.g., *Rochette et al.*, 1999]. However, mechanical effects related with a flow that can evolve from simple shear near the margins to pure shear towards the core [*Féménias et al.*, 2004], may be able to reorient the larger mineral surfaces to a plane approximately perpendicular to the flow direction (abnormal fabric). *Kratinová et al.* [2006] reproduced similar fabrics from analogue modeling. When a magma supply exceeds the rate of space creation, forceful magma emplacement responsible for space creation can also produce abnormal AMS fabrics [*Stevenson*, 2009]. The great majority of the sites show angular deviations within the limit recognized as "normal" fabrics. Few exceptions are observed and even for these ones the angular deviations are mainly due to differences in dip and not in direction (compare values of α and β in Table 2).

[54] In order to visualize the AMS pattern at the FZD-scale, K_1 axes from fabric 3 and K_3 axes from fabrics 2 and 3 were all rotated to the same reference frame, which is the average attitude of the dyke (40°/90°, Figures 11a and 11b). The magnetic foliation strikes on average parallel to the dyke, but dip varies among sites: towards the dyke core very close to the dyke border and toward the dyke wall elsewhere (see Figure 11c). Such a symmetrical imbrication indicates a vertical movement of the magma. K_1 from Fabric 3 is mostly along the foliation plunge, which in this case is consistent with the flow inferred from the foliation. The observed decrease of the magnetic foliation dip from margin to dyke core suggests the superposition of a pure shear component on simple shear [*Raposo and Ernesto*, 1995; *Féménias et al.*, 2004; *Kratinová et al.*, 2006]. This latter geometry has been interpreted as indicating upward flow, which means that the opposite geometry indicates downward flow (achieved very close the margin). However, this is very unlikely at the depth of emplacement of the FZD because: 1. The chilled margins show that flow was frozen very fast close to dyke margins, where flow is supposed to be mostly upward; and 2. downward flow is inhibited by the pressure gradient, which tends to close the fracture that the magma is forcefully injecting. Therefore, alternative explanations must be sought. It has been shown that rigid inclusions in a viscous fluid do not always follow the predictions by *Jeffery* [1922]. This is the case of mixtures of simple and pure shears [*Marques and Coelho*, 2003], slip at inclusion/matrix interface [e.g., *Ildefonse and Mancktelow*, 1993; *Marques and Coelho*, 2001; *Mancktelow et al.*, 2002; *Ceriani et al.*, 2003; *Marques and Bose*, 2004; *Marques et al.*, 2005b; *Schmid and Podladchikov*, 2004; *Marques et al.*, 2007] and confined flow [*Marques et al.*, 2005a], which can produce stable fabrics dipping toward or opposite to shear sense. It has also been shown that shearing of mixtures of melt and crystals can produce foliations that dip towards shear sense [e.g., *Batchelor*, 1967; *Holtzman et al.*, 2003; *Holtzman et al.*, 2005]. Moreover, due to magma pressure and dyke geometry, the first stages of intrusion are characterized by changes of the stress regime responsible for the opening and propagation of the dyke tip [e.g., *Rubin and Pollard*, 1988; *Rubin*, 1995; *Curewitz and Karson*, 1998; *Mériaux and Jaupart*, 1998; *Gudmundsson and Loetveit*, 2005]. The mechanisms that produce a stable foliation dipping towards shear sense can

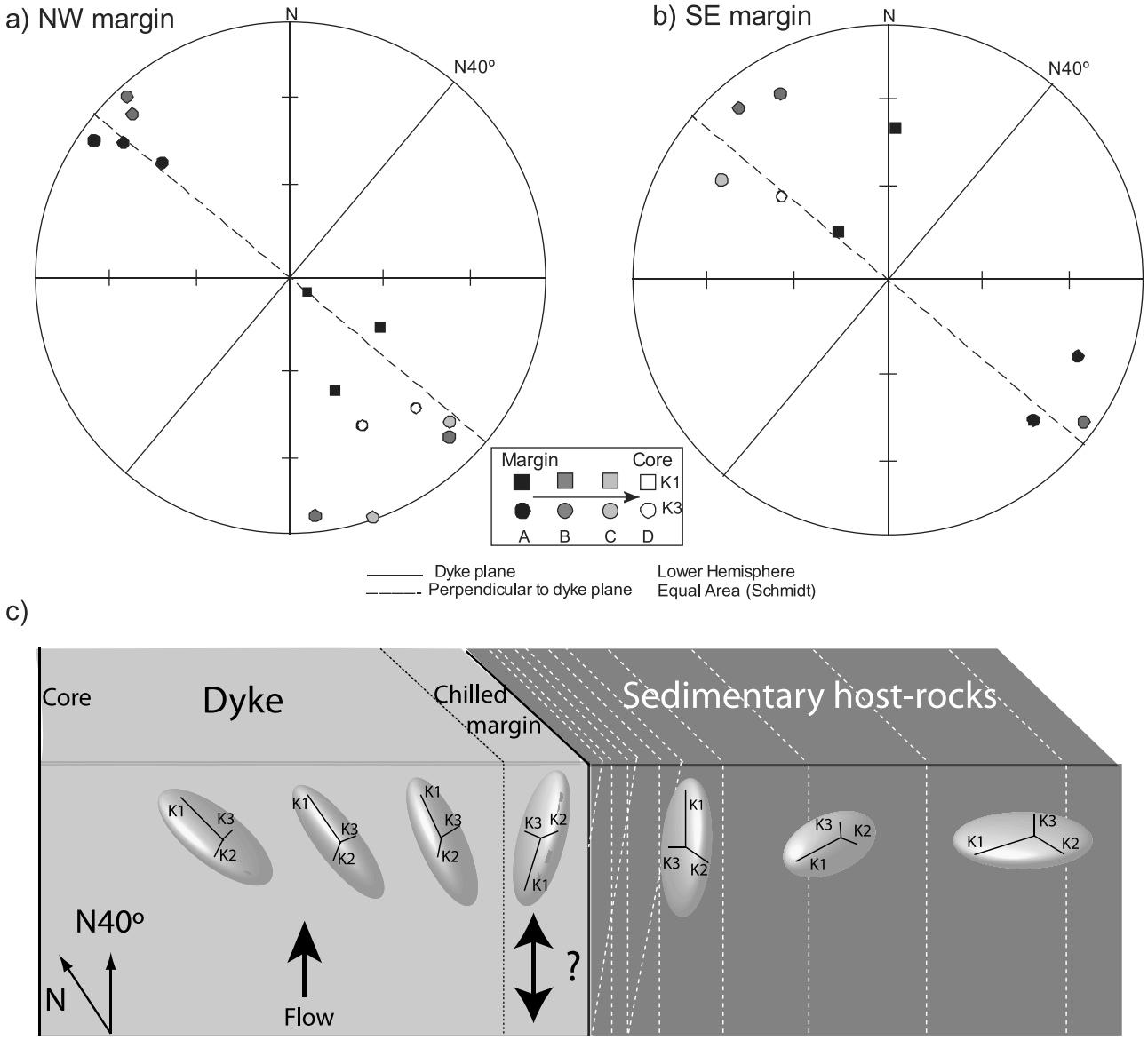

Figure 11. Equal area stereographic projections illustrating the evolution of the AMS ellipsoid along the profiles of K_1 (squares) for fabric 3 and K_3 (circles) for fabrics 2 and 3. Projections for sites located near the (a) NW and (b) SE margins. (c) Nonscaled sketch resuming the evolution of the AMS ellipsoids for dolerite dyke and sedimentary host rocks with the distance to the contact; white dashed lines at the sedimentary host rocks represent the planar discontinuities with increasing concentration towards the contact. Black dashed line within dyke delimits the chilled margin where fabrics 1 and 3 are observed.

be responsible for an AMS foliation that can be erroneously interpreted as downward flow in dykes. Other possible explanations for the origin of the magnetic foliation dipping toward dyke core are being investigated by our group.

9. Conclusions

[55] From the work here presented it is possible to conclude that: 1. High-temperature lamellae oxidation-exsolution promotes an enrichment of low-Ti titanomagnetite (main magnetic carrier) and an increase of SD grains towards inner domains of the dyke. 2. Metasomatic processes, coeval with later cooling stages, also led to an effective decrease of the primary ferromagnetic carriers and for the appearance of a secondary fine-grained ferromagnetic mineral aggregates from hydrous-phyllosilicates. 3. Such high and low temperature chemical processes are responsible for the presence of composite AMS fabrics. In addition, pAARM measurements reveal that such composite fabrics are controlled by populations with distinct coercivities. 4. Comparison between AMS and pAARM reveal that the imbrication between magnetic foliation and dyke plane is more reliable than the orientation of AMS maximum principal axes (which rather results from an intersection lineation). 5. The forceful intrusion of this thick dyke induced deformation in the host sedimentary rocks in two typical ways, homogeneous flattening and/or folding of sedimentary strata. AMS records such mechanical effects as a gradual transition from

a bedding-parallel magnetic foliation away from the dyke to a dyke-parallel magnetic foliation close to the contacts. 6. Dominant subvertical magma flow near the margins is representative of the magma flow from mantle to surface and is consistent with the structures observed at the host rocks and the magnetic fabric within the dyke borders. 7. The spatial arrangement of quartz veins bordering the dyke in the northernmost segment and their geometrical relationship with the dyke indicates a preintrusive to synintrusive, sinistral component of strike slip.

Appendix A: Description of Host Rocks at Stations Where Samples Were Collected

[56] Station FZ1 encompasses two profiles, one at site FZ1S-A where sedimentary samples were collected far from the dyke (~400 m), and the other at FZ1S-B, close to the SE contact. At FZ1S-A, we sampled for the characteristic sedimentary fabric, though not affected by the intrusive processes but by the older regional deformation. It consists of open folds with hinges plunging approximately 10° towards azimuth 118°. At FZ1S-B host rocks near the contact are folded, with bedding striking 40° in azimuth (i.e., subparallel to the dyke trend) and reaching 70° in dip. Close to the contact the host rocks show penetrative subvertical planar anisotropy subparallel to the dyke (40°/90°; Figure 1c).

[57] At FZ2S and within 100 m from the dyke, bedding dips 22° towards azimuth 210°. Two main families of penetrative planar discontinuities are visible, with attitudes 70°/60°S (azimuth strike/dip) and 220°/86°NW. These two families of planar discontinuities gradually decrease in intensity with increasing distance to contact, which is subvertical and trends 40° in azimuth (Figure 1c).

[58] At FZ8S and in the first 6 m bordering the dyke, bedding cannot be recognized and planar discontinuities are rare, being limited to scarce subvertical fractures perpendicular to the dyke. Farther from the dyke, bedding becomes conspicuous, slightly dipping (6°) SE, and some planar discontinuities systems appear, the most penetrative comprising subvertical planes running parallel to the dyke.

[59] At the NW margin of FZ9D and close to the contact, bedding in carbonates is folded with axial planes subparallel to dyke and hinge slightly plunging towards NW. Farther from the contact, bedding dips gently SE as at FZ8S. Two main families of planar discontinuities were recognized, a penetrative one with attitude 40°/78° and another one 315°/75° (Figure 1c).

[60] At FZ11S, bedding dips 8°SW between the two dykes, 5°NE southeast of dyke FZ11D-A, and is horizontal northwest of dyke FZ11D-B.

[61] **Acknowledgments.** This is a contribution to research projects TEAMINT (POCTI/CTE/48137/2002) and AMS PROGRESS (PTDC/CTE-GIX/098696/2008). Fundação Calouste Gulbenkian is acknowledged for funding. We thank M. Le Goff for technical assistance during experimental work. We thank the Laboratório Nacional de Energia e Geologia at S. Mamede Infesta and Fernanda Guimarães for technical support with microprobe analysis. We thank the Laboratoire des Mécanismes et Transferts en Géologie at Toulouse, namely Philippe de Perceval, Thierry Aigouy, and Sophie Gouy for technical assistance with SEM analyses. We are very grateful to two anonymous reviewers for helpful and detailed comments.

References

Aarab, E. M., A. Rahimi, and G. Rocci (1994), Un exemple de différenciation transverse: Le Grand Dyke de Foum Zguid (Anti-Atlas, Maroc), *C.R. Acad. Sci., Ser. II*, *319*, 209–215.

Ade-Hall, J. M., H. C. Palmer, and T. P. Hubbard (1971), The magnetic and opaque petrological response of basalts to regional hydrothermal alteration, *Geophys. J. R. Astron. Soc.*, *24*, 137–174.

Almqvist, B. S. G., A. M. Hirt, V. Schmidt, and D. Dietrich (2009), Magnetic fabrics of the Morcles Nappe complex, *Tectonophysics*, *466*, 89–100.

Aubourg, C., P. Rochette, J.-F. Stéfan, M. Popoff, and C. Chabert-Pelline (1999), The magnetic fabric of weakly deformed Late Jurassic shales from the southern subalpine chains (French Alps): Evidence for SW-directed tectonic transport direction, *Tectonophysics*, *307*, 15–31.

Aubourg, C., G. Tshoso, B. Le Gall, H. Bertrand, J.-J. Tiercelin, A. B. Kampunzu, J. Dyment, and M. Modisi (2008), Magma flow revealed by magnetic fabric in the Okavango giant dyke swarm, Karoo igneous province, northern Botswana, *J. Volcanol. Geotherm. Res.*, *170*, 247–261.

Baer, G. (1995), Fracture propagation and magma flow in segmented dykes: field evidences and fabric analyses, Makhtesh Ramon, Israel, in *Physics and Chemistry of Dykes*, pp. 125–140, edited by G. Baer and A. Heimann, Balkema, Rotterdam, Neth.

Baksi, A. K., and D. A. Archibald (1997), Mesozoic igneous activity in the Maranhao province, northern Brazil: $^{40}Ar/^{39}Ar$ evidence for separate episodes of basaltic magmatism, *Earth Planet. Sci. Lett.*, *151*, 139–153.

Batchelor, G. K. (1967), *An Introduction to Fluid Mechanics*, 615 pp., Cambridge Univ. Press, Cambridge, U. K.

Besse, J., and V. Courtillot (2002), Apparent and true polar wander and the geometry of the geomagnetic field over the last 200 Myr, *J. Geophys. Res.*, *107*(B11), 2300, doi:10.1029/2000JB000050.

Blanchard, J. P., P. Boyer, and C. Gagny (1979), Un nouveau critère de sens de mise en place dans une caisse filonienne: Le "pincement" des minéraux aux éponte, *Tectonophysics*, *53*, 1–25.

Blumenfeld, P., and J.-L. Bouchez (1988), Shear criteria in granite and migmatite deformed in the magmatic and solid states, *J. Struct. Geol.*, *10*, 361–372.

Borradaile, G. J., and D. Gauthier (2003), Interpreting anomalous magnetic fabrics in ophiolite dikes, *J. Struct. Geol.*, *25*, 171–182.

Borradaile, G. J., and B. Henry (1997), Tectonic applications of magnetic susceptibility and its anisotropy, *Earth Sci. Rev.*, *42*, 49–93.

Borradaile, G. J., and D. Gauthier (2006), Magnetic studies of magma-supply and sea-floor metamorphism: Troodos ophiolite dikes, *Tectonophysics*, *418*, 75–92, doi:10.1016/j.tecto.2005.12.014.

Borradaile, G. J., and D. Gauthier (2007), Reply to discussion of "Magnetic studies of magma-supply and sea-floor metamorphism: Troodos ophiolite dikes" (Borradaile and Gauthier, 2005), *Tectonophysics*, *433*, 149–153, doi:10.1016/j.tecto.2006.12.005.

Borradaile, G. J., and M. Jackson (2004), Anisotropy of magnetic susceptiblity (AMS): Magnetic petrofabrics of deformed rocks, in *Magnetic Fabric: Methods and Applications*, *Geol. Soc. Spec. Publ.*, *238*, pp. 361–380, edited by F. Martín-Hernández et al., Geol. Soc., London, U.K.

Callot, J. P., and X. Guichet (2003), Rock texture and magnetic lineation in dykes: A simple analytical model, *Tectonophysics*, *366*, 207–222.

Callot, J. P., L. Geoffroy, C. Aubourg, J. P. Pozzi, and D. Mege (2001), Magma flow directions of shallow dykes from the East Greenland volcanic margin inferred from magnetic fabric studies, *Tectonophysics*, *335*, 313–329, doi:10.1016/S0040-1951(01)00060-9.

Callot, J.-P., L. Geoffroy, and C. Aubourg (2007), Comment on "Magnetic studies of magma-supply and sea-floor metamorphism: Troodos ophiolite dikes," *Tectonophysics*, *433*, 141–147, doi:10.1016/j.tecto.2006.12.004.

Cañón-Tapia, E., and E. Herrero-Bervera (2009), Sampling strategies and the anisotropy of magnetic susceptibility of dykes, *Tectonophysics*, *466*, 3–17.

Ceriani, S., N. S. Mancktelow, and G. Pennacchioni (2003), Analogue modeling of the influence of shape and particle/matrix interface lubrication on the rotational behavior of rigid particles in simple shear, *J. Struct. Geol.*, *25*, 2005–2021.

Chadima, M., P. Pruner, S. Šlechta, T. Grygar, and A. M. Hirt (2006), Magnetic fabric variations in Mesozoic black shales, Northern Siberia, Russia: Possible paleomagnetic implications, *Tectonophysics*, *418*, 145–162.

Chadima, M., V. Cajz, and P. Týcová (2009), On the interpretation of normal and inverse magnetic fabric in dikes: Examples from the Eger Graben, NW Bohemian Massif, *Tectonophysics*, *466*, 47–63.

Cifelli, F., M. Mattei, M. Chadima, S. Lenser, and A. M. Hirt (2009), The magnetic fabric in "undeformed clays": AMS and neutron texture analyses from the Rif Chain (Morocco), *Tectonophysics*, *466*, 79–88.

Correa-Gomes, L. C., C. R. Souza Filho, C. J. F. N. Martins, and E. P. Oliveira (2001), Development of symmetrical and asymmetrical fabrics in sheet-like igneous bodies: The role of magma flow and wall-rock displacements in theoretical and natural cases, *J. Struct. Geol.*, *23*, 1415–1428.

Curewitz, D., and J. A. Karson (1998), Geological consequences of dike intrusion at mid-ocean ridge spreading centers, in *Faulting and Magmatism at Mid-Ocean Ridges*, *Geophys. Monogr.*, *106*, pp. 117–136, edited by W. R. Buck et al., AGU, Washington, D. C.

Day, R., M. Fuller, and V. A. Schmidt (1977), Hysteresis properties of titanomagnetites: Grain size and compositional dependence, *Phys. Earth Planet. Inter.*, *13*, 260–267.

Dunlop, D. J. (2002), Theory and application of the Day plot (*Mrs*/*Ms* versus *Hcr*/*Hc*) 1: Theoretical curves and tests using titanomagnetite data, *J. Geophys. Res.*, *107*(B3), 2056, doi:10.1029/2001JB000486.

Dunlop, D. J., and Ö. Özdemir (1997), *Rock Magnetism: Fundamentals and Frontiers*, 573 pp., Cambridge Univ. Press, Cambridge, U.K.

Dunning, G. R., and J. P. Hodych (1990), U/Pb zircon and baddeleyite ages for the Palisades and Gettysburg sills of the northeastern United States: Implications for the age of the Triassic/Jurassic boundary, *Geology*, *18*, 795–798.

Féménias, O., H. Diot, T. Berzad, A. Gauffriau, and D. Demaiffe (2004), Asymmetrical to symmetrical magnetic fabric of dikes: Paleo-flow orientations and Paleo-stresses recorded on feeder-bodies from the Motru Dike Swarm (Romania), *J. Struct. Geol.*, *26*, 1401–1418.

Ferré, E. C. (2002), Theoretical models of intermediate and inverse AMS fabrics, *Geophys. Res. Lett.*, *29*(7), 1127, doi:10.1029/2001GL014367.

Geoffroy, L., J. P. Callot, C. Aubourg, and M. Moreira (2002), Magnetic and plagioclase linear fabric discrepancy in dykes: A new way to define the flow vector using magnetic foliation, *Terra Nova*, *14*, 183–190.

Graham, J. W. (1954), Magnetic susceptibility anisotropy, an unexploited petrofabric element, *Bull. Geol. Soc. Am.*, *65*, 1257–1258.

Gudmundsson, A. (2006), How local stresses control magma-chamber ruptures, dyke injections, and eruptions in composite volcanoes, *Earth Sci. Rev.*, *79*, 1–31.

Gudmundsson, A., and I. F. Loetveit (2005), Dyke emplacement in a layered and faulted rift zone, *J. Volcanol. Geotherm. Res.*, *144*, 311–328.

Hailwood, E. A. (1975), The palaeomagnetism of Triassic and cretaceous rocks from Morocco, *Geophys. J. R. Astron. Soc.*, *41*, 219–235.

Hailwood, E. A., and J. G. Mitchell (1971), Paleomagnetic and radiometric dating results from Jurassic intrusions in South Morocco, *Geophys. J. R. Astron. Soc.*, *24*, 351–364.

Henry, B. (1997), The magnetic zone axis: A new element of magnetic fabric for the interpretation of the magnetic lineation, *Tectonophysics*, *271*, 325–329.

Henry, B., and M. Meurisse (1978), Mesures d'anisotropie de susceptibilité magnétique dans une ophite Pyrénéenne: détermination du mode de mise en place, *Mem. BRGM*, *91*, 457–463.

Henry, B., et al. (2009), Repeated granitoid intrusions during the Neoproterozoic along the western boundary of the Saharan metacraton, Eastern Hoggar, Tuareg shield, Algeria: An AMS and U-Pb zircon age study, *Tectonophysics*, *474*, 417–434.

Herrero-Bervera, E., E. Cañón-Tapia, G. P. L. Walker, and J. C. Guerrero-Garcia (2002), The Nuuanu and Wailua giant landslides: Insights from palaeomagnetic and anisotropy of magnetic susceptibility (AMS) studies, *Phys. Earth Planet. Inter.*, *129*, 83–98.

Hext, G. (1963), The estimation of second-order tensor, with related tests and designs, *Biometrika*, *50*, 353–357.

Hildenbrand, A., P. Madureira, F. O. Marques, I. Cruz, B. Henry, and P. Silva (2008), Multi-stage evolution of a subaerial volcanic ridge over the last 1.3 Myr: S. Jorge Island, Azores Triple Junction, *Earth Planet. Sci. Lett.*, *273*, 289–298.

Hirt, A. M., M. Julivert, and J. Soldevila (2000), Magnetic fabric and deformation in the Navia-Alto Sil slate belt, northwestern Spain, *Tectonophysics*, *320*, 1–16.

Hollard, E. A. (1973), La mise en place au Lias des dolerites dans le Paléozoique moyen du NE des plains du bassin de Tindouf (Sud de l'Anti/Atlas Central, Maroc), *C.R. Seances Acad Sci., Ser. D*, *277*, 553–556.

Holtzman, B. K., D. L. Kohlstedt, M. E. Zimmerman, F. Heidelbach, T. Hiraga, and J. Hustoft (2003), Melt segregation and strain partitioning: Implications for seismic anisotropy and mantle flow, *Science*, *301*, 1227–1230.

Holtzman, B. K., D. L. Kohlstedt, and J. P. Morgan (2005), Viscous energy dissipation and strain partitioning in partially molten rocks, *J. Petrol.*, *46*, 2569–2592, doi:10.1093/petrology/egi065.

Hrouda, F., Š. Táborská, K. Schulmann, J. Jezek, and D. Dolejš (1999), Magnetic fabric and rheology of comingled magmas in the Nasavrky Plutonic Complex (E. Bohemia): Implications for intrusive strain regime and emplacement mechanism, *Tectonophysics*, *307*, 93–111.

Hrouda, F., M. Chlupacova, and J. K. Novak (2002), Variations in magnetic anisotropy and opaque mineralogy along a kilometer deep profile within a vertical dyke of the syenogranite porphyry at Cínovec (Czech Republic), *J. Volcanol. Geotherm. Res.*, *113*, 37–47.

Ildefonse, B., and N. S. Mancktelow (1993), Deformation around rigid particles: The influence of slip at the particle/matrix interface, *Tectonophysics*, *221*, 345–359.

Jackson, M. (1991), Anisotropy of magnetic remanence: A brief review of mineralogical sources, physical origins, and geological applications, and comparison with susceptibility anisotropy, *Pure Appl. Geophys.*, *136*, 1–28, doi:10.1007/BF00878885.

Jackson, M., W. Gruber, J. Marvin, and S. K. Banerjee (1988), Partial anhysteretic remanence and its anisotropy: Applications and grain-size dependence, *Geophys. Res. Lett.*, *15*, 440–443.

Jeffery, G. B. (1922), The motion of ellipsoidal particles immersed in a viscous fluid, *Proc. R. Soc. London, Ser. A*, *102*, 161–179.

Jelínek, V. (1978), Statistical processing of magnetic susceptibility measured in groups of specimens, *Stud. Geoph. Geod.*, *22*, 50–62.

Jelínek, V. (1981), Characterization of the magnetic fabric of rocks, *Tectonophysics*, *79*, 63–67, doi:10.1016/0040-1951(81)90110-4.

Jelínek, V. (1993), Theory and measurement of the anisotropy of isothermal remanent magnetization of rocks, *Travaux Geophys.*, *37*, 124–134.

Kent, D.V., P. E. Olsen, and W. K. Witte (1995), Late Triassic-earliest Jurassic geomagnetic polarity sequence and paleolatitudes from drill cores in the Newark Rift Basin, eastern North America, *J. Geophys. Res.*, *100*, 14,965–14,998.

Khan, M. A. (1962), The anisotropy of magnetic susceptibility of some igneous and metamorphic rocks, *J. Geophys. Res.*, *67*, 2874–2885.

Knight, K. B., S. Nomade, P. R. Renne, A. Marzoli, H. Bertrand, and N. Youbie (2004), The Central Atlantic Magmatic Province at the Triassic-Jurassic boundary: Paleomagnetic and $^{40}Ar/^{39}Ar$ evidence from Morocco for brief, episodic volcanism, *Earth Planet. Sci. Lett.*, *228*, 143–160.

Knight, M. D., and G. P. L. Walker (1988), Magma flow directions in dikes of the Koolau complex, Oahu, determined from magnetic fabric studies, *J. Geophys. Res.*, *93*, 4301–4319, doi:10.1029/JB093iB05p04301.

Krasa, D., and E. Herrero-Bervera (2005), Alteration induced changes of magnetic fabric as exemplified by dykes of the Koolau volcanic range, *Earth Planet. Sci. Lett.*, *240*, 445–453.

Kratinová, Z., P. Závada, F. Hrouda, and K. Schulmann (2006), Nonscaled analogue modeling of AMS development during viscous flow: A simulation on diapir-like structures, *Tectonophysics*, *418*, 51–61.

Lattard, D., R. Engelmann, A. Kontny, and U. Sauerzapf (2006), Curie temperatures of synthetic titanomagnetites in the Fe-Ti-O system: Effects of composition, crystal chemistry, and thermomagnetic methods, *J. Geophys. Res.*, *111*, B12S28, doi:10.1029/2006JB004591.

Leblanc, M. (1974), Le grand dyke de dolérites de l'Anti.Atlas et le magmatisme jurassique du Sud-Marocain, *C.R. Acad. Sci., Ser. D*, *278*, 2943–2946.

Lowrie, W. (1990), Identification of ferromagnetic minerals in a rock by coercivity and unblocking temperature properties, *Geophys. Res. Lett.*, *17*, 159–162.

Lyakhovsky, V., Y. Ben-Zion, and A. Agnon (1997), Distributed damage, faulting, and friction, *J. Geophys. Res.*, *102*, 27,635–27,649, doi:10.1029/97JB01896.

Mancktelow, N. S., L. Arbaret, and G. Pennacchioni (2002), Experimental observations on the effect of interface slip on rotation and stabilization of rigid particles in simple shear and a comparison with natural mylonites, *J. Struct. Geol.*, *24*, 567–585.

Marcais, J., and G. Choubert (1956), *Les Grands Traits de la Géologie du Maroc: Lexique Stratigraphique du Maroc*, *Introduction Géologique*, 168 pp., Dir. Mines Géol., Rabat, Maroc.

Marques, F. O., and S. Coelho (2001), Rotation of rigid elliptical cylinders in viscous simple shear flow: Analogue experiments, *J. Struct. Geol.*, *23*, 609–617.

Marques, F. O., and S. Bose (2004), Influence of a permanent low-friction boundary on rotation and flow in rigid inclusion/viscous matrix systems from an analogue perspective, *Tectonophysics*, *382*, 229–245, doi:10.1016/j.tecto.2004.01.004.

Marques, F. O., and S. Coelho (2003), 2D shape preferred orientations of rigid particles in transtensional viscous flow, *J. Struct. Geol.*, *25*, 841–854.

Marques, F. O., R. Taborda, and J. Antunes (2005a), 2D rotation of rigid inclusions in confined bulk simple shear flow: a numerical study, *J. Struct. Geol.*, *27*, 2171–2180. doi:10.1016/j.jsg.2005.08.008.

Marques, F. O., R. Taborda, and J. Antunes (2005b), Influence of a low-viscosity layer between rigid inclusion and viscous matrix on inclusion

rotation and matrix flow: A numerical study, *Tectonophysics*, *407*, 101–115, doi:10.1016/j.tecto.2005.07.005.

Marques, F. O., D. W. Schmid, and T. B. Andersen (2007), Applications of inclusion behaviour models to a major shear zone system: The Nordfjord-Sogn detachment zone in western Norway, *J. Struct. Geol.*, *29*, 1622–1631.

Martin, D. L., A. E. M. Nairn, H. C. Noltimier, M. H. Petty, and T. J. Schmitt (1978), Paleozoic and Mesozoic paleomagnetic results from Morocco, *Tectonophysics*, *44*, 91–114.

Marzoli, A., P. R. Renne, E. M. Piccirillo, M. Ernesto, G. Bellieni, and A. De Min (1999), Extensive 200 million-year-old continental flood basalts of the central Atlantic magmatic province, *Science*, *284*, 616–618, doi:10.1126/science.284.5414.616.

Masquelin, H., T. Aïfa, R. Muzio, E. Hallot, G. Veroslavsky, and L. Bonnevalle (2009), The Cuaró Mesozoic doleritic dyke swarm, southern Paraná basin, Uruguay: Examples of superimposed magnetic fabrics?, *C. R. Geosci.*, *341*, 1003–1015, doi:10.1016/j.crte.2009.07.004.

May, P. R. (1971), Pattern of Triassic-Jurassic diabase dikes around the North Atlantic in the context of predrift position of the continents, *Geol. Soc. Am. Bull.*, *82*, 1285–1292.

Mériaux, C., and C. Jaupart (1998), Dike propagation through an elastic plate, *J. Geophys. Res.*, *103*, 18,295–18,314.

Mériaux, C., J. R. Lister, V. Lyakhovsky, and A. Agnon (1999), Dyke propagation with distributed damage of the host rock, *J. Geophys. Res.*, *165*, 177–185.

Moreira, M., L. Geoffroy, and J.-P. Pozzi (1999), Ecoulement magmatique dans les dykes du point chaud des Açores: Étude préliminaire par anisotropie de susceptibilité magnétique ASM dans l'Île de San Jorge, *C. R. Acad. Sci., Ser. IIa Sci. Terre Planetes*, *329*, 15–22, doi:10.1016/S1251-8050(99)80222-5.

Nomade, S., H. Theveniaut, Y. Chena, A. Pouclet, and C. Rigollet (2000), Paleomagnetic study of French Guyana Early Jurassic dolerites: Hypothesis of a multistage magmatic event, *Earth Planet. Sci. Lett.*, *184*, 155–168.

Olsen, P. E. (1999), Giant lava flows, mass extinctions, and mantle plumes, *Science*, *284*, 604–605.

Olsen, P. E., D. V. Kent, M. Et-Touhami, and J. H. Puffer (2003), Cyclo-, magneto-, and bio-stratigraphic constraints on the duration of the CAMP event and its relationship to the Triassic-Jurassic boundary, in *The Central Atlantic Magmatic Province: Insights From Fragments of Pangea*, *Geophys. Monogr. Ser.*, vol. 136, edited by W. E. Hames et al., pp. 7–32, AGU, Washington, D. C.

O'Reilly, W. (Ed.) (1984), *Rock and Mineral Magnetism*, 220 pp., CRC Press, Boca Raton, Fla.

Palencia-Ortas, A. (2004), Estudio Paleomagnético de rocas de edad Jurásica de La Península Ibérica y sur de Marruecos, Ph.D Thesis, Universidad Complutense de Madrid, Spain.

Palencia-Ortas, A., M. L. Osete, R. Vegas, and P. F. Silva (2006), Paleomagnetic study of the Messejana-Plasencia dyke (Portugal and Spain): A lower Jurassic paleopole for the Iberian plate, *Tectonophysics*, *420*, 455–472.

Petrovský, E., and A. Kapička (2006), On determination of the Curie point from thermomagnetic curves, *J. Geophys. Res.*, *111*, B12S27, doi:10.1029/2006JB004507.

Potter, D. K. (2004), A comparison of anisotropy of magnetic remanence methods: A user's guide for application to paleomagnetism and magnetic fabric studies, 21, in *Magnetic Fabric: Methods and Applications*, *Geol. Soc. Spec. Publ.*, vol. 238, edited by F. Martín-Hernández et al., pp. 361–380, Geol. Soc., London, U.K.

Potter, D. K., and A. Stephenson (1988), Single-domain particles in rocks and magnetic fabric analysis, *Geophys. Res. Lett.*, *15*, 1097–1100.

Raposo, M. I., and T. S. Berquó (2008), Tectonic fabric revealed by AARM of the Proterozoic mafic dike swarm in the Salvador city (Bahia State): São Francisco Craton, NE Brazil, *Phys. Earth Planet. Inter.*, *167*, 179–194.

Raposo, M., and M. Ernesto (1995), Anisotropy of magnetic susceptibility in the Ponta-Grossa dyke swarm (Brazil) and its relationship with magma flow direction, *Phys. Earth Planet. Inter.*, *87*, 183–196.

Raposo, M., I. McReath, and M. S. D'Agrella-Filho (2006), Magnetic fabrics, rock magnetism, cathodoluminescence, and petrography of apparently undeformed Bambui carbonates from São Francisco Basin (Minas Gerais State, SE Brazil): An integrated study, *Tectonophysics*, *418*, 111–130, doi:10.1016/j.tecto.2005.12.016.

Rochette, P. (1988), Inverse magnetic fabric carbonate bearing rocks, *Earth Planet. Sci. Lett.*, *90*, 229–237.

Rochette, P., C. Aubourg, and M. Perrin (1999), Is this magnetic fabric normal? A review and case studies in volcanic formations, *Tectonophysics*, *307*, 219–234.

Rubin, A. M. (1995), Propagation of magma-field cracks, *Annu. Rev. Earth Planet. Sci.*, *23*, 287–336.

Rubin, A. M., and D. D. Pollard (1988), Origins of blade-like dikes in volcanic rifts zones, in *Volcanism in Hawaii*, edited by R. W. Decker et al., *U.S. Geol. Surv. Prof. Pap.*, 1350, 1449–1470.

Schmid, D. W., and Y. Y. Podladchikov (2004), Are isolated stable rigid clast in shear zones equivalent to voids?, *Tectonophysics*, *384*, 233–242.

Schmidt, M. W. (1992), Amphibole composition in tonalite as a function of pressure: An experimental calibration of the Al-in-hornblende barometer, *Contrib. Mineral. Petrol.*, *110*, 304–310.

Schott, J. J., R. Montigny, and R. Thuizat (1981), Paleomagnetism and potassium-argon age of the Messejana Dike (Portugal and Spain): Angular limitation to the rotation of the Iberian Peninsula since the Middle Jurassic, *Earth Planet. Sci. Lett.*, *53*, 457–470.

Sebai, A., G. Feraud, H. Bertrand, and J. Hanes (1991), $^{40}Ar/^{39}Ar$ dating and geochemistry of tholeiitic magmatism related to the early opening of the Central Atlantic rift, *Earth Planet. Sci. Lett.*, *104*, 455–472.

Silva, P. F., F. O. Marques, J. M. Miranda, B. Henry, and A. Mateus (2001), Anisotropy of magnetic susceptibility constraints on Variscan obduction processes in the Bragança Massif (NE Portugal), *Tectonophysics*, *341*, 95–119, doi:10.1016/S0040-1951(01)00194-9.

Silva, P. F., F. O. Marques, B. Henry, A. Mateus, N. Lourenço, and J. M. Miranda (2004), Preliminary results of a study of magnetic properties in the Foum-Zguid dyke (Morocco), *Phys. Chem. Earth*, *29*, 909–920, doi:10.1016/j.pce.2004.01.016.

Silva, P. F., B. Henry, F. O. Marques, P. Madureira, and J. M. Miranda (2006a), Paleomagnetic study of the Great Foum Zguid dyke (Southern Morocco): A positive contact test related to metasomatic processes, *Geophys. Res. Lett.*, *33*, L21301, doi:10.1029/2006GL027498.

Silva, P. F., B. Henry, F. O. Marques, A. Mateus, P. Madureira, N. Lourenço, and J. M. Miranda (2006b), Variation of magnetic properties in sedimentary rocks hosting the Foum Zguid dyke (southern Morocco): Combined effects of re-crystallization and Fe-metasomatism, *Earth Planet. Sci. Lett.*, *241*, 978–992.

Silva, P. F., B. Henry, F. O. Marques, E. Font, A. Mateus, R. Vegas, J. M. Miranda, R. Palomino, and A. Palencia-Ortas (2008), Magma flow, exsolution processes, and rock metasomatism in the Great Messejana-Plasencia dyke (Iberian Peninsula), *Geophys. J. Intern.*, *175*, 806–824, doi: 10.1111/j.1365-246X.2008.03920.x.

Smith, B. M. (1987), Consequences of the maghemitization on the magnetic properties of submarine basalts: Synthesis of previous works and results concerning basement rocks from mainly DSDP legs 51 and 52, *Phys. Earth Planet. Inter.*, *46*, 206–226.

Stephenson, A., S. Sadikum, and D. Potter (1986), A theoretical and experimental comparision of the susceptibility and remanence in rocks and minerals, *Geophys. J. R. Astron. Soc.*, *84*, 185–200.

Stevenson, C. (2009), The relationship between forceful and passive emplacement: The interplay between tectonic strain and magma supply in the Rosses Granitic Complex, NW Ireland, *J. Struct. Geol.*, *31*, 270–287, doi:10.1016/j.jsg.2008.11.009.

Schumacher, J. C. (1997), The estimation of ferric iron in electron microprobe analysis of amphiboles: Appendix II to the nomenclature of amphiboles, *Miner. Mag. 61*, 295–321.

Tarling, D. H., and F. Hrouda (1993), *The Magnetic Anisotropy of Rocks*, Chapman and Hall, London, U.K.

Trindade, R. I. F., M. I. B. Raposo, M. Ernesto, and R. Siqueira (1999), Magnetic susceptibility and partial anhysteretic remanence anisotropies in the magnetite-bearing granite pluton of Tourão, NE Brazil, *Tectonophysics*, *314*, 443–468.

Wilson, R. I., S. E. Haggerty, and N. D. Watkins (1968), Variation of palaeomagnetic stability and other parameters in a vertical traverse of a single Icelandic lava, *Geophys. J. R. Astr. Soc.*, *16*, 79–96.

E. Font, N. Lourenço, and F. O. Marques, Instituto Dom Luís, Universidade de Lisboa, P-1749-016 Lisboa, Portugal.

B. Henry, Paléomagnétisme, Institut de Physique du Globe de Paris, CNRS, 4 Ave. de Neptune, Saint-Maur F-94107, France.

A. M. Hirt, Laboratory of Natural Magnetism, Institute of Geophysics, ETH Zurich, CH-8092, Zurich, Switzerland.

P. Madureira, Departamento de Geociências, Centro de Geofísica de Évora, Universidade Évora, P-7000-671 Évora, Portugal.

P. F. Silva, Departamento de Engenharia Civil, Instituto Superior de Engenharia de Lisboa, P-1959-007 Lisboa, Portugal. (pmfsilva@fc.ul.pt)